Zero Change CMOS Microring Modulators at 1550 nm: Modeling and Characterization

Marc de Cea Falcó

Degree thesis

Physical Optics and Electronics Group, Research Laboratory of Electronics
Massachusetts Institute of Technology

Escola Tècnica Superior d'Enginyeria de Telecomunicació de Barcelona
Universitat Politècnica de Catalunya

Submitted in partial fulfillment
of the requirements for the degree in
Telecommunications Science and Technology

Supervised by:
Prof. Rajeev J. Ram
Prof. Jose Antonio Lázaro

June 2017

Abstract

Zero change CMOS Microring Modulators at 1550 nm: Modeling and characterization

by Marc de Cea Falcó

While optical communications are the standard solution for long haul communications, its adoption for short range (i.e, intra- and inter-chip interconnects and metro-area) transmission systems, where a considerable increase in data rates and a decrease in power consumption is to be gained, has been hampered mainly because the high cost associated to the fabrication of discrete optical components. The integration of photonic components in a single substrate, in what is known as silicon photonics, arises as a promising solution to overcome this limitation.

Specifically, zero change CMOS silicon photonics, in which photonic components are fabricated in state of the art commercial microelectronic foundries without any change in the fabrication flow, therefore not modifying the transistor yield, enables the monolithic integration of electronics and photonics at a very low cost. Nevertheless, this comes at an expense in the control of the fabrication process and, as such, in the performance of the devices.

It is of paramount importance, then, to carefully design, model and optimize these photonic components and test them experimentally. It is the object of this thesis to do so for one of the photonic components necessary for optical communications: modulators.

To avoid high optical losses and achieve high optical confinement, the whispering gallery modes of silicon rings (with radii in the order of μm) are exploited, and effective modulation is achieved by changing the carrier density in the silicon by means of pn junctions.

In this thesis, high speed (25 Gbps) modulation at a working wavelength of 1550 nm is reported for the first time in a zero-change CMOS platform, and it is also demonstrated that this photonics platform can be readily used for low temperature ($\sim$ 4 K) applications. A complete model of a silicon microring modulator that includes nonlinear effects (which can have an important detrimental effect in the device performance) is also derived, and from it power handling capabilities of these modulators are determined.

By realizing high-speed an efficient optical modulators at the telecommunications wavelength, the potential of this CMOS photonics platform for addressing the future demands in the telecom and datacom systems by the fabrication of high scale electronic-photonic systems has been unveiled.

Resum

Zero change CMOS Microring Modulators at 1550 nm: Modeling and characterization

per Marc de Cea Falcó

Mentre les comunicacions òptiques són la solució estàndard per a comunicacions de llarga distància, l'adopció daquestes per a transmissió de curt abast (és a dir, inter- i intra-xip i àrea metropolitana), que permetria un increment considerable en les velocitats de transmissió i un decrement en el consum, ha estat limitada principalment per l'alt cost associat a la fabricació de components òptics discrets. La integració de múltiples dispositius fotònics en un mateix substrat, en el que es coneix com a *silicon photonics*, és una solució prometedora a aquesta limitació.

En concret, el *zero change CMOS silicon photonics*, en el que els components òptics es fabriquen en fundicions microelectròniques comercials sense cap modificació al procés de fabricació i, per tant, sense reduir la quantitat de transistors operatius, permet la integració monolítica d'electrònica i fotònica a baix cost. Això implica, però, un menor control en el procés de fabricació i, en conseqüència, en el rendiment dels dispositius.

És per tant primordial dissenyar, modelar i optimitzar aquests components amb cura i caracteritzar-los experimentalment. L'objectiu d'aquesta tesi és fer això per a un dels dispositius fotònics imprescindibles per a les comunicacions òptiques: el modulador.

Per a evitar altes pèrdues i aconseguir gran confinament òptic, els modes òptics d'anells de silici (amb radis de l'ordre de μm) coneguts com a *whispering gallery* són empleats, i mitjançant el canvi de la densitat de portadors al silici a través d'unions pn s'aconsegueix modular la llum.

En aquesta tesi, modulació a alta velocitat (25 Gbps) a una longitud d'ona de 1550 nm és demostrada per primera vegada en una plataforma *zero change CMOS*, i també es prova la possibilitat d'utilitzar aquesta plataforma per a aplicacions a baixa temperatura ($\sim$ 4 K). També es deriva un model complet d'un modulador ressonant de silici incloent efectes no lineals (que poden tenir un gran efecte en el rendiment del dispositiu), i a partir d'aquest es determinen els límits en la potència entrant en aquests moduladors.

Mitjançant la fabricació de moduladors òptics eficients i amb gran ample de banda a longituds d'ona pròpies de telecomunicació, el potencial de la plataforma òptica *zero change CMOS* per a cobrir la futura demanda d'alta velocitat de transmissió en sistemes de *datacom* i telecomunicacions ha estat descoberta.

Resumen

Zero change CMOS Microring Modulators at 1550 nm: Modeling and characterization

por Marc de Cea Falcó

Aunque las comunicaciones ópticas son la solución estándar para comunicaciones de largo alcance, su adopción para transmisión de corto alcance (es decir, inter- e intra-chip y área metropolitana), que permitiría un considerable incremento en la velocidad de transmisión y una reducción en el consumo, ha estado limitada principalmente por el alto coste asociado a la fabricación de componentes ópticos discretos. La integración de múltiples dispositivos fotónicos en un mismo sustrato, en lo que se conoce como *silicon photonics*, es una solución prometedora a esta limitación.

En concreto, el *zero change CMOS silicon photonics*, en el cual los componentes ópticos se fabrican en fundiciones microelectrónicas comerciales sin ninguna modificación en el proceso de fabricación y, por tanto, sin reducir la cantidad de transistores operativos, permite la integración monolítica de electrónica y fotónica a bajo coste. Esto implica, sin embargo, un menor control en el proceso de fabricación y, en consecuencia, en el rendimiento de los dispositivos. Es primordial, por tanto, diseñar, modelar y optimizar estos dispositivos con precisión y caracterizarlos experimentalmente. El objetivo de esta tesis es hacer esto para uno de los componentes fotónicos imprescindibles en las comunicaciones ópticas: el modulador.

Para evitar altas pérdidas y conseguir un gran confinamiento óptico, los modos ópticos de un anillo de silicio (con radios en el orden de μm) conocidos como *whispering gallery* son empleados, y la modulación óptica se obtiene mediante el cambio de la densidad de portadores en el silicio a través de uniones pn.

En esta tesis, modulación a alta velocidad (25 Gbps) a una longitud de onda de 1550 nm es demostrada por primera vez en una plataforma *zero change CMOS*, y también se prueba la posibilidad de utilizar esta plataforma para aplicaciones a baja temperatura ($\sim$ 4 K). También se deriva un modelo completo de un modulador resonante de silicio incluyendo efectos no lineales (que pueden tener un gran efecto en el rendimiento del dispositivo), y a partir de este se determinan los límites en la potencia entrante en este.

Mediante la fabricación de moduladores ópticos eficientes y con gran ancho de banda a longitudes de onda de telecomunicaciones, el potencial de la plataforma óptica *zero change CMOS* para cubrir la futura demanda de alta velocidad de transmisión en sistemas de *datacom* y telecomunicaciones ha sido descubierta.

Acknowledgements

Many thanks to professor Rajeev J. Ram for accepting me in the group and for his guidance. Every conversation we had was stimulating and revealing.

Special thanks to doctor Amir H. Atabaki for his mentorship, for his help and for many hours of discussion. Nothing of what I have done would have been possible without his expertise.

Thanks to all the people in the Physical Optics and Electronics group at MIT, to this group of brilliant scientists which are also good friends.

At UPC, I would like to thank professor Jose Antonio Lázaro for co-advising this thesis and for offering me this amazing, life-changing opportunity. Thanks also to CFIS for its help in making my stay in Boston possible.

Thanks also to all my friends, the new ones I met in Boston and the old ones from Barcelona. All of you made me feel like home.

Finally, great thanks to all my family, for always believing in me, for making me who I am today, for, essentially, loving me.

List of original publications

1. **M. de Cea**, A. H. Atabaki, L. Alloatti, M. T. Wade, M. Popovic and R. J. Ram. A Thin Silicon Photonic Platform for Telecommunication Wavelengths. Accepted for the *European Conference on Optical Communication (ECOC)*, September 2017.

Contents

Abstract iii

Resum iv

Resumen v

Acknowledgements vi

List of original publications vii

List of Figures x

List of Tables xiii

Abbreviations xiv

1 Introduction 1
- 1.1 The potential of photonic integration . . . 1
- 1.2 Silicon photonics . . . 2
- 1.3 Zero change CMOS silicon photonics . . . 4
- 1.4 Thesis outline . . . 6

2 Theoretical Background 7
- 2.1 Optical modulators . . . 7
  - 2.1.1 Performance metrics for optical modulators . . . 8
- 2.2 Silicon optical modulators: working principle . . . 8
- 2.3 Silicon microring modulators . . . 11
  - 2.3.1 Theory . . . 11
  - 2.3.2 Operation modes and trade-offs . . . 14
- 2.4 Silicon modulators: a brief review . . . 15
- 2.5 Summary . . . 17

3 Thin silicon zero-change CMOS microring modulator characterization at 1550 nm 18
- 3.1 Modulator geometry . . . 18
- 3.2 DC characterization . . . 20
- 3.3 High speed characterization . . . 21
- 3.4 Transmission over moderate distances . . . 22
  - 3.4.1 Chirp parameter . . . 23

3.4.2 Eye diagrams . . . 26
3.5 Optical link . . . 26
3.6 Conclusion . . . 28

4 Nonlinearities in microring modulators **30**
4.1 Relevant nonlinear effects in silicon resonant modulators . . . 31
4.2 Model derivation . . . 32
4.2.1 Loss rate . . . 33
4.2.2 Microring resonance wavelength . . . 35
4.2.3 Dynamic equations . . . 36
4.3 A simple case . . . 39
4.4 Power handling capabilities of silicon ring modulators . . . 41
4.4.1 Design considerations . . . 42
4.4.2 Operation conditions considerations . . . 47
4.4.2.1 The importance of initialization . . . 48
4.4.2.2 The best operational point . . . 50
4.5 Summary . . . 52

5 Low Temperature Operation of Silicon Microring Modulators **53**
5.1 Low temperature operation of silicon photonic devices: concerns . . . 54
5.1.1 Carrier freeze-out . . . 54
5.1.2 Modulation considerations . . . 55
5.2 IV characteristics . . . 56
5.3 Summary . . . 57

6 Conclusions and future work **59**

Bibliography **61**

List of Figures

1.1 Silicon photonics 2013-2024 market forecast [1]. 3
1.2 Electro-optic system on a single chip [2]. (a) Micrograph of the chip. (b) Transmitter and receiver banks. (c) From left to right, micrograph of the grating coupler, photodetector and modulator. 5

2.1 Free carrier density manipulation mechanisms [3]. (a) Carrier injection: Applying a forward bias causes free electrons and holes from the highly doped p and n regions to be injected into the intrinsic region. (b) Carrier depletion. Applying a reverse bias to the pn junction changes the width of the depletion region. 10
2.2 Schematic diagram of a silicon microring modulator. The silicon waveguide has a curvature to avoid higher order modes to couple into the ring and obtain better modal confinement [4]. The coupling coefficients used in the scattering matrix formulism are shown in blue. 11
2.3 Experimental transmission spectra of a silicon microring modulator. . . . 13
2.4 Working principle of a ring modulator. By applying a voltage, the resonance wavelength of the ring changes (blue and red curves) due to the plasma dispersion effect. As the laser wavelength is fixed at λ_l, the output power is different at each applied voltage (P_1 and P_0). Important parameters of the modulation such as IL and ER are also depicted. . . . 14
2.5 (a) Geometry of the first silicon ring resonator modulator [5]. (b) Cross section of a vertical pn junction, which runs parallel to the top and bottom surfaces of the waveguide. (c) Cross section of a horizontal (or lateral) pn junction, which runs perpendicular to the top and bottom surfaces of the waveguide. (d) Cross section (top) and plan (bottom) of an interdigitated pn junction. (b), (c) and (d) are taken from [6]. 16

3.1 Modulator geometry. (a) Top view of the 20 μm diameter resonant modulator. Sections of the p and n regions and the metal contacts are shown. (b) Micrograph of the front (top) and back (bottom) of the modulator. Grating couplers (GC), ground (G) and Signal (S) electrodes and optical cavity are recognizeable. (c) Cross section of the WGM profile of the device shown in (a). 19
3.2 DC characterization of the ring modulator. (a) Experimental setup showing the electrical (red) and optical (black) paths. Power meters are used to obtain the transmission for each wavelength. FBS = fiber optical beam splitter. (b) Transmission vs wavelength for different bias voltages. The resonance shift is approximately 20 pm/V at -0.5 V bias. 20

3.3 Modulator bandwidth measurement. (a) Experimental setup showing the electrical (red) and optical (black) paths. A VNA with the driving signal at port 1 and the signal out of a commercial photodetector connected to the modulator at port 2 is used to obtain the frequency response. (b) Small-signal frequency response at -2V bias. The 3dB bandwidth is around 14GHz. 21
3.4 Experimental setup showing the electrical (red) and optical (black) paths for the acquisition of eye diagrams. 22
3.5 Eye diagrams for different data rates and driving voltages. (a) 2.10 dB ER and 0.26 dB IL eye at 25 Gbps and 1.6 V_{pp}. (b) 6.23 dB ER and 0.5 dB IL eye at 25 Gbps and 3.6 V_{pp}. (c) 3.24 dB ER and 0.2 dB IL eye at 32 Gbps and 3.6 V_{pp}. 23
3.6 Chirp characterization. (a) Experimental setup showing the electrical (red) and optical (black) paths. (b) Chirp parameter vs bias voltage. Different curves show different detunings from the resonance wavelength of the resonator. 25
3.7 Experimental setup for the acquisition of eye diagrams after propagation over SMF. 26
3.8 12.5 Gbps eye diagrams after moderate distance propagation. A 1.6 V_{pp}, $2^{11}-1$ PRBS driving signal and 2 V reverse bias are used. (a) Recorded eye diagram after 50 km propagation over SMF. (b) Recorded eye diagram after 75 km propagation over SMF. 27
3.9 Link measurement. (a) Experimental setup for the link measurement showing the electrical (red) and optical (black) paths. (b) 15 Gbps eye diagram. The modulator driving voltage is 3.6 V_{pp} at -2 V bias, while the detector is biased at 20 V. 28

4.1 System temporal behavior for $\lambda_0 = 1567.2\ nm, \lambda_l = 1567.1\ nm$, $P_{in} = 5\ mW$ and no modulation. Self modulation is observed. 40
4.2 Self modulation cycle. The black line represents the fixed laser wavelength, and the blue line depicts the modulator resonance that moves due to nonlinear effects. Red arrows show the direction of the resonance shift. A double arrow represents a rapid shift, while a single arrow means slow evolution. 41
4.3 Free carrier parameter vs heating parameter for all the different simulated geometries. 44
4.4 Heating parameter dependence with geometry. (a) Varying radius and height with fixed width. (b) Varying width and height with fixed radius. . 45
4.5 Heating parameter dependence with varying ring height. 45
4.6 Maximum absorbed power P_{abs} as a function of doping density for 3 mW and 1 μW input optical powers and $\lambda_l = \lambda_0$. Equal doping for the p and n regions is assumed. 46
4.7 Comparison between different initialization methods. (a) Minimum achievable transmission as a function of the input power for the fixed wavelength initialization (red) and for the proposed wavelength sweep initialization (blue). (b) Transmission as a function of wavelength for a 1 mW input power for the fixed wavelength initialization (red) and for the proposed initialization (blue). The cold resonance wavelength is set at $\lambda_0 = 1557.2\ nm$. 49

4.8 Optimum operational point. (a) Maximum attainable value of the figure of merit (blue, left axis) and wavelength at which this value is reached (red, right axis) as a function of input power. The inset shows the evolution of the figure of merit as a function of the stop laser wavelength for different input powers. (b) Evolution of the ER (black), IL (red) and figure of merit (black) as a function of the stop laser wavelength. The input power is set to 1 mW, and the cold resonance wavelength is set to $\lambda_0 = 1557.2\ nm$. 51

5.1 IV characteristics of a 1550 nm zero-change CMOS microring modulator at different temperatures. Diode-like characteristics are obtained at all tested temperatures. 57

List of Tables

4.1 Geometrical parameters swept in the ring geometry analysis 43

5.1 Hole and electron conductivity effective masses (in units of the free electron mass m_0) and mobilities (in $cm^2/V \cdot s$) in silicon at 4K and 300K for doping densities $N_a = N_d = 1 \times 10^{18}\ cm^{-3}$. 56

Abbreviations

ASE	**A**mplified **S**pontaneous **E**mission
BW	**B**and**W**idth
BER	**B**it **E**rror **R**ate
CMOS	**C**omplementary **M**etal-**O**xide-Semiconductor
EDFA	**E**rbium **D**oped **F**iber **A**mplifier
ER	**E**xtinction **R**atio
FCA	**F**ree **C**arrier **A**bsorption
FEM	**F**inite **E**lements **M**ethod
FCD	**F**ree **C**arrier **D**ensity
FSR	**F**ree **S**pectral **R**ange
GC	**G**rating **C**ouplers
IL	**I**nsertion **L**oss
ISI	**I**nter**S**ymbol **I**nterference
MRM	**M**icro**R**ing **M**odulator
MZI	**M**ach **Z**ender **I**nterferometer
PRBS	**P**seudo **R**andom **B**inary **S**equence
SMF	**S**ingle **M**ode **F**iber
SOI	**S**ilicon **O**n **I**nsulator
SNSPD	**S**uperconducting **N**anowire **S**ingle **P**hoton **D**etector
TPA	**T**wo **P**hoton **A**bsorption
VNA	**V**ector **N**etwork **A**nalyzer
WDM	**W**avelength **D**ivision **M**ultiplexing
WGM	**W**hispering **G**allery **M**ode

Chapter 1

Introduction

1.1 The potential of photonic integration

The impressive increase in the data traffic over the last two decades poses an even more impressive challenge to the information and communication technologies (ICT) industry. As the demands of consumers in terms of bandwidth and power consumption have led the traditional microelectronics approach to reach its performance limits, optical data transmission is arising as a very promising solution. In fact, fiber-optic data transmission is now the standard solution for long-haul data transmission systems, in which the high-bandwidth, low attenuation and robustness to interference outperforms the old copper cabling used for this purpose.

But optical data transmission is not yet a solution adopted for on-chip and chip-to-chip communication, mainly because, up to now, copper interconnects have been able to cover the bandwidth needs at a low cost. But as these needs increase, the limitations due to increased attenuation, crosstalk and dispersion become more and more important. As in long reach applications, optical interconnects postulate as the solution for these limitations [7], thanks to its inherent high bandwidth density (achievable through the use of wavelength division multiplexing (WDM)), low loss and low interference, which translates into a lower power consumption, an idea first introduced by Joseph Goodman in 1981 [8].

One of the main limitations for the widespread adoption of optical interconnects is its high cost compared to copper. This is not a problem for long haul communication (where

the gross of the cost is in the fiber-optic installation), but it is a limiting factor in intra- and inter-chip data communication systems, where the cost pressure is on the hardware needed for interconnection. In this sense, the ability to integrate all the necessary photonic components on a common substrate would allow the miniaturization of photonic systems, therefore reducing manufacturing costs and simplifying the fabrication process. This is known as integrated photonics, and it was first introduced by Miller in 1969 [9].

But the potential of integrated photonics goes far beyond interconnects and optical communication networks, as the integration of multiple optical functions in a single photonic chip allows the large-scale manufacturing of small, low cost, scalable, complex and powerful advanced optical systems with a wide range of applications.

1.2 Silicon photonics

The highest level of integration is achieved with monolithic integration, in which all the optical elements are incorporated in a single substrate, and silicon is one of the most promising candidates for this purpose.

Silicon is an inexpensive, well understood material, with a high quality native oxide and excellent thermal and electric properties. But what makes silicon photonics be regarded as the key technology for the future telecom and datacom industry is the fact that it is the semiconductor used in the microelectronics industry and, as such, all the knowledge, processes, infrastructure and technologies developed over the last century for microelectronics can be readily exploited.

In particular, the ability to use the complementary metal-oxide-semiconductor (CMOS) fabrication processes developed for the microelectronics industry allows for high-volume, low cost production, opening up the possibility of applying photonics to areas where the high-cost of conventional photonic elements prevented its deployment.

The ability to achieve strong optical confinement at the telecommunications wavelengths through the use of silicon and silicon oxide structures in what is known as Silicon On Insulator (SOI) [10] processes is another reason why silicon photonics is so appealing, as it offers a way to fabricate low loss optical waveguides and very compact photonic

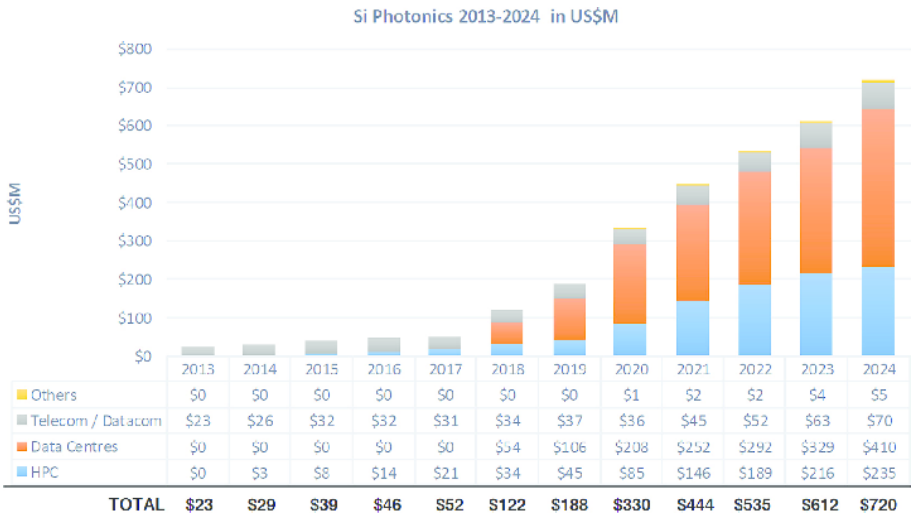

	2013	2014	2015	2016	2017	2018	2019	2020	2021	2022	2023	2024
Others	$0	$0	$0	$0	$0	$0	$0	$1	$2	$2	$4	$5
Telecom / Datacom	$23	$26	$32	$32	$31	$34	$37	$36	$45	$52	$63	$70
Data Centres	$0	$0	$0	$0	$0	$54	$106	$208	$252	$292	$329	$410
HPC	$0	$3	$8	$14	$21	$34	$45	$85	$146	$189	$216	$235
TOTAL	**$23**	**$29**	**$39**	**$46**	**$52**	**$122**	**$188**	**$330**	**$444**	**$535**	**$612**	**$720**

FIGURE 1.1: Silicon photonics 2013-2024 market forecast [1].

devices. In fact, this observation (first reported by Soref in 1985) was what started to bring attention to silicon as a substrate for integrated photonics [11].

It is also important to note that the fact of using silicon as a platform for building photonic components opens up the possibility to integrate in the same chip not only photonic components, but also electronics, in what is known as electro-optic integration. While the use of other substrates like gallium arsenide (GaAs) might be appealing for photonic integration, the immediate possibility of electro-optic integration is only present in silicon.

The incredible potential of silicon photonics as a key technology has been recognized by both academia and industry. In 2004, the United States Defense Advanced Research Projects Agency (DARPA) launched a 4 year project on electronic and photonic integrated circuits (EPIC) in silicon, in what was a major investment in silicon photonics. The International Technology Roadmap for Semiconductors (ITRS) recognized silicon photonics as a key technology for six of its seven focus areas. Electronics giants such as Intel, IBM, Hewlett Packard and STMicroelectronics have made huge investments to drive progress in silicon photonics.

Not only this, but silicon photonics has already turned into a commercial technology, with companies such as Luxtera [12] or Acacia Communications [13] manufacturing 100 Gbps transceivers for the datacenter and telecommunications markets. Figure 1.1 shows the US market forecast for the silicon photonics industry, reaching an impressive

$700 million by 2024 [1], when the investment will come from webcom companies like Facebook or Microsoft.

1.3 Zero change CMOS silicon photonics

Nevertheless, silicon is not the optimal photonic material, mainly because it has an indirect bandgap that prevents the possibility to build efficient laser sources [14] and because, being a centrosymmetric material, the typical second order nonlinearities exploited in other substrates to build active photonic devices do not exist [15].

Thus, to enhance the performance of silicon photonic platforms the typical approach is to incorporate III-V materials with better optical performance such as indium phosphide (InP) in what is known as hybrid silicon photonics [16]. Although this technique allows for the fabrication of optimized photonic devices, the need to use a modified CMOS process increases considerably the manufacturing cost and, more importantly, it reduces the transistor yield, preventing a successful integration of optics and photonics in the same chip and, ultimately, the commercial adoption of this technology.

An alternative approach is to design and fabricate the photonic devices complying strictly with the rules of commercial microelectronic foundries to avoid any modification to the CMOS fabrication process, in what is known as *zero-change CMOS* [17]. Although this comes at an expense in the performance of the photonic components (not only because additional materials cannot be added, but also because some control over the fabrication process is lost) it maintains the high transistor yield , thus making possible to build complex electronic circuits in the same chip as optics. Moreover, not using modified processes allows for a reduced cost of fabrication.

This approach has proven successful, and a complete photonic component toolbox has been demonstrated in commercial SOI microelectronic foundries [17], with the perfomance of each single device increasing since then [18, 19]. A monolithic microprocessor built using the zero-change CMOS approach which used optical interconnects to communicate with the memory was demonstrated in GlobalFoundries 45 nm 12SOI CMOS process [2]. The chip integrated over 70 million transistors and 850 photonic components, confirming the validity of the zero-change approach to build high performance electro-optic systems on a single chip. Figure 1.2 shows the fabricated chip.

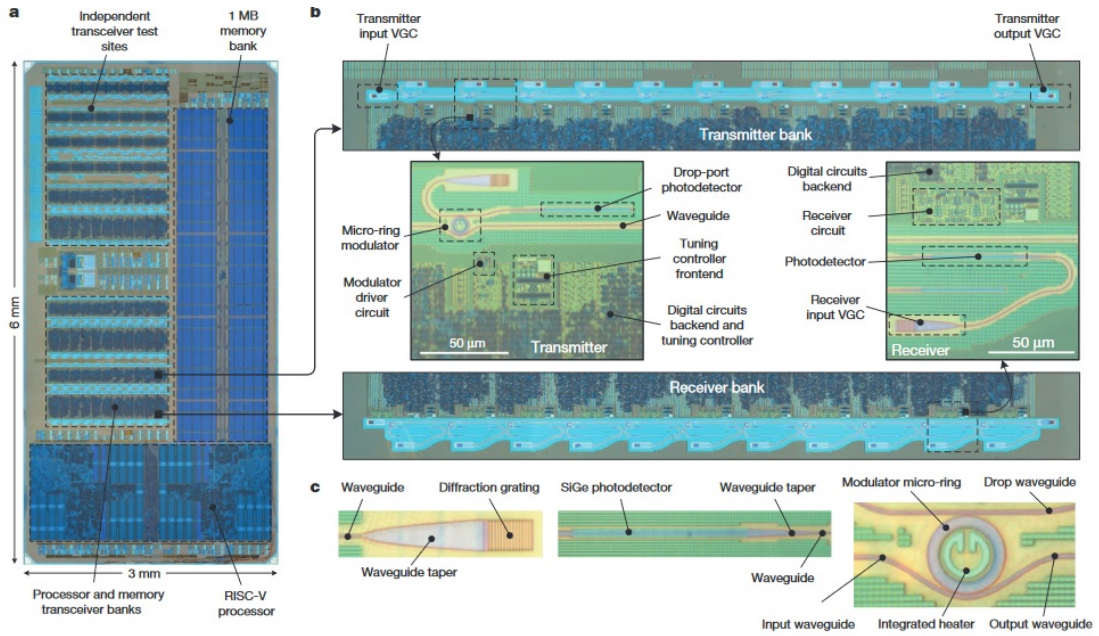

FIGURE 1.2: Electro-optic system on a single chip [2]. (a) Micrograph of the chip. (b) Transmitter and receiver banks. (c) From left to right, micrograph of the grating coupler, photodetector and modulator.

It is clear, then, that the zero-change CMOS approach is a promising solution that enables electro-optic integration of complex systems in a single chip, paving the way for the implementation of high speed, low cost and low power consumption photonic interconnects for the datacom and telecom industries.

This thesis deals with the study and characterization of one of the fundamental components of optical links and interconnects: the optical modulator. A new zero-change CMOS resonant modulator designed at a working wavelength of 1550 nm is experimentally characterized for high speed operation, and its suitability for low temperature (4K) operation as an interface between cryogenic operating devices and its associated room temperature electronics is also evaluated. Furthermore, nonlinearities arising in this kind of modulators are modeled to evaluate its power handling capabilities.

1.4 Thesis outline

The remainder of this thesis is organized as follows:

- In chapter 2, the basic theory necessary to understand this thesis is reviewed. The working principle of silicon microring modulators is presented and the principal performance metrics of optical modulators are discussed.
- In chapter 3, a complete characterization of a zero-change CMOS microring modulator with a working wavelength of 1550 nm is presented. The challenges of using the thin (< 100 nm) silicon layer used in advanced microelectronic foundries such as the ones used for high performance computing are discussed and addressed.
- In chapter 4, a theoretical model to describe and study non linearities in silicon resonant structures is derived. This model is then used to evaluate the power handling capabilities of microring modulators for different designs and operation conditions.
- In chapter 5, the suitability of the zero-change CMOS microring modulators for low temperature (4K) operation is evaluated, and some preliminary experiments are performed.
- Chapter 6 concludes the thesis and suggests future work.

Chapter 2

Theoretical Background

In this chapter, the theoretical background necessary to understand this thesis is presented, with a strong focus on silicon resonant modulators as they are the main topic of this thesis.

Familiarity with semiconductor physics (mainly pn junctions) and waveguiding (mainly modal confinement and propagation, first order perturbation theory and modal coupling) is assumed in this chapter and throughout the entire thesis. [20], [21] and [10] are given as references for these topics.

2.1 Optical modulators

An optical modulator is a device that converts bits carried by an electrical signal (electrical bits) to bits carried by a light wave (optical bits). To do so, an incident light wave is modified using the electrical signal (which is normally used to change some physical parameter of the medium that carries the light, that is, the waveguide), so that an electrical '1' lets the light pass unattenuated while an electrical '0' attenuates it. Note that this is a simple On-Off Keying modulation, in which a bit '1' is signaled by the presence of light and a bit '0' is signaled by the absence of light [1].

[1] While more sophisticated modulation schemes have been effectively implemented in optical modulators [22], the vast majority use this approach.

2.1.1 Performance metrics for optical modulators

There are several metrics used to characterize and evaluate an optical modulator:

- Modulation bandwidth (BW): It is related with the ability of a modulator to encode data at a certain bit rate, and is defined as the frequency at which the modulation amplitude is 3dB below the amplitude at low frequencies.
- Extinction Ratio (ER): It is the ratio between the optical intensity of the bit '1' and that of the bit '0' at the output of the modulator, and is usually expressed in dB.
- Insertion Loss (IL): It takes into account the optical power lost when the modulator is added into the photonic link due to reflection and absorption.
- Optical bandwidth: It is related with the wavelength range of the incident light in which the modulator is able to operate without any tuning.
- Power consumption: Usually quantified as the mean energy necessary to modulate one bit, the target is set to less than 100 fJ/bit [23].

An ideal modulator would have an infinitely high modulation bandwidth, ER and optical bandwidth, while featuring zero IL and power consumption.

2.2 Silicon optical modulators: working principle

As already discussed in the previous chapter, silicon photonics is a promising solution to overcome the current limitations in the datacom and telecom industries. Being the optical modulator a critical component for photonic communication links, considerable effort has been carried out by the scientific community to engineer high speed and low power consumption modulators in silicon.

The physical effects that are usually exploited by semiconductor material modulators (i.e., Pockels effects, Kerr effects and Franz-Keldysh effects [10]), in which an applied electric field changes the real or the imaginary part of the refractive index of the waveguide carrying the light, cannot be used for effective modulation in silicon because they

are too weak [24]. Another possibility would be to use the thermooptic effect, i.e., the change in the refractive index due to a change in temperature, but although this phenomenon is strong in silicon (as it has a high thermooptic coefficient) it is too slow for the high data rates required in modern communications [25].

The effect in which the majority of high speed silicon optical modulators rely on is the plasma dispersion effect, in which a change in the concentration of free carriers changes the real and imaginary part of the refractive index [10] of the material. Although this effect was initially described by a simple Drude model, Soref and Benett [24] used experimentally derived absorption spectra to obtain the refractive index changes and obtained the following expressions at 1.55 μm, usually known as Soref's equations:

$$\Delta n = -(8.8 \times 10^{-22} \times \Delta N_e + 8.5 \times 10^{-18} \times \Delta N_h^{0.8}) \tag{2.1}$$

$$\Delta \alpha = 8.5 \times 10^{-18} \times \Delta N_e + 6 \times 10^{-18} \times \Delta N_h^{0.8}) \tag{2.2}$$

Where Δn is the change in the refractive index, $\Delta \alpha$ is the change in the absorption coefficient in cm^{-1} and ΔN_e (ΔN_h) is the change in the density of free electrons (holes) in cm^{-3}.

So, for example, a change in the carrier density of 5×10^{17} cm^{-3} results in a change in refractive index $\Delta n = -1.66 \times 10^{-3}$. As will be discussed later, this induced change in the refractive index of the medium carrying the light can be used for light modulation. It is important to note that the change in the refractive index is accompanied by a change in the absorption coefficient α due to linear absorption of free carriers, which is detrimental in terms of optical loss and, as will be discussed later in this thesis, generates chirp.

Different approaches can be used to generate the necessary changes in the free carrier density (ΔN_e and ΔN_h), mainly carrier injection and carrier depletion. These schemes are represented in schematically in Figure 2.1. Although the carrier injection operation features a higher modulation efficiency (meaning that for the same applied voltage, a bigger change in the refractive index is generated compared to carrier depletion), carrier depletion silicon modulators are preferred because they can support higher modulation

speeds and have better thermal dissipation properties, as will be discussed later in this chapter.

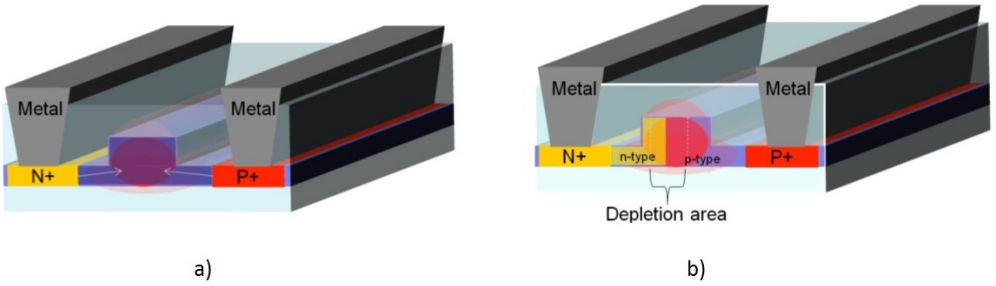

FIGURE 2.1: Free carrier density manipulation mechanisms [3]. (a) Carrier injection: Applying a forward bias causes free electrons and holes from the highly doped p and n regions to be injected into the intrinsic region. (b) Carrier depletion. Applying a reverse bias to the pn junction changes the width of the depletion region.

So far, we have discussed how an induced change in the free carrier density changes the refractive index of the silicon waveguide that is carrying the light we want to modulate. To convert the change in the refractive index to a change in the output intensity two different approaches exist. The first approach consists in using the refractive index change to control the relative phase between two propagating waves to generate either constructive or destructive interference, with Mach-Zehnder interferometer (MZI) configurations being typically used for this purpose [26]. An alternative approach is to use resonant structures such as rings, in which the change in the refractive index changes the resonace condition (i.e., the resonance wavelength) so that the device switches between the on- and off-resonance states.

While MZIs feature higher optical bandwidth and are less sensitive to temperature and fabrication variations, microring modulators (MRM) have a smaller footprint (μm diameter compared to mm lengths for MZI), lower cost and a much lower power consumption, so they are usually considered superior to MZI to fulfill the demanding specifications the datacom and telecom industries will face in the future.

2.3 Silicon microring modulators

2.3.1 Theory

A typical ring modulator consists of one bus waveguide coupled to a single modulated ring, as illustrated in Fig. 2.2. Part of the incident light is coupled into the ring, which after travelling along the length of the modulator couples back into the waveguide. The interference between the light travelling along the bus waveguide and the light coupled back from the ring determines the output power of the modulator.

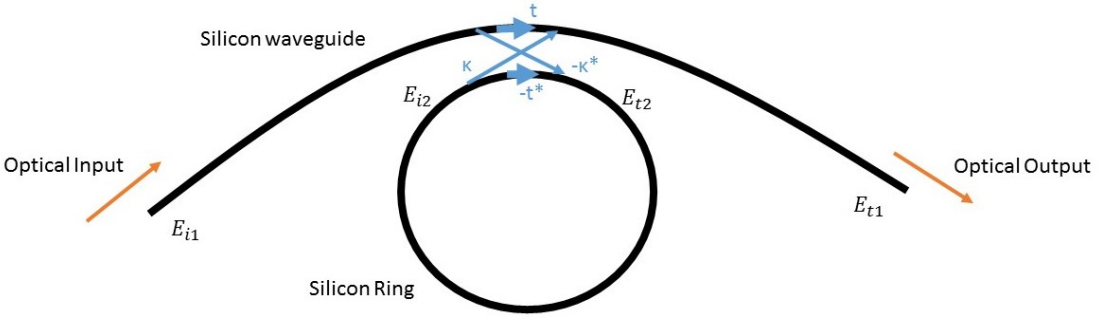

FIGURE 2.2: Schematic diagram of a silicon microring modulator. The silicon waveguide has a curvature to avoid higher order modes to couple into the ring and obtain better modal confinement [4]. The coupling coefficients used in the scattering matrix formulism are shown in blue.

There are two main (and equivalent) ways of describing the relationship between the incident and the transmitted waves in an optical modulator: by the use of first order perturbation theory [21] and by the use of the scattering matrix formulism [27]. As the first order perturbation theory will be used later in this thesis, in this section we will use the scattering matrix formulism, which states that the modulator can be seen as a two port circuit:

$$\begin{pmatrix} E_{t1} \\ E_{t2} \end{pmatrix} = \begin{pmatrix} t & \kappa \\ -\kappa^* & t^* \end{pmatrix} \begin{pmatrix} E_{i1} \\ E_{i2} \end{pmatrix} \tag{2.3}$$

Where the mode amplitudes E are normalized and consistent with Fig. 2.2. t and κ are coupling coefficients and * denotes the complex conjugate.

With this, the transmitted power in the steady state (normalized to the input power) can be easily derived [27]:

$$P_{t1} =\mid E_{t1} \mid^2 = \frac{\alpha^2 + \mid t \mid^2 -2\alpha \mid t \mid cos(\theta + \phi_t)}{1 + \alpha^2 \mid t \mid^2 -2\alpha \mid t \mid cos(\theta + \phi_t)} \tag{2.4}$$

Where α is the loss coefficient of the ring ($\alpha = 1$ corresponding to no loss), ϕ_t the phase introduced by the coupling and θ is the phase change undergone by the light after doing a round trip along the disk and is given by:

$$\theta = \frac{wL}{c} = kn_{eff}2\pi r = \frac{4\pi^2 n_{eff} r}{\lambda} \tag{2.5}$$

Where L is the perimeter of the ring, r is its radius and n_{eff} is the effective index of the waveguide.

From equations 2.4 and 2.5 is is straightforward to find the resonnance wavelengths of the ring modulator, in which the output optical power is minimal:

$$\lambda_r = \frac{4\pi^2 n_{eff} r}{2\pi m - \phi_t} \quad ; \quad m \in \mathbf{R} \tag{2.6}$$

According to what has been derived above, the optical transmission spectra of a ring modulator will consist of a series of lorentzian notches located at the resonnance wavelengths of the ring, which are dictated by the radius r of the resonator and its effective index n_{eff}. The minimum transmission will be:

$$P_{tmin} = \frac{(\alpha - \mid t \mid)^2}{(1 - \alpha \mid t \mid)^2} \tag{2.7}$$

Note that the minimum transmitted power will be 0 only when $\alpha =\mid t \mid$, a condition that is known as "critical coupling". α is related to the optical losses induced by the ring, while $\mid t \mid$ is related to the losses due to the coupling between the waveguide and the ring. At the critical coupling condition, the optical losses of the ring are the same as the losses due to the coupling between waveguide and ring, so $\alpha =\mid t \mid$. When $\alpha >\mid t \mid$, the ring is said to be in the undercoupled regime (where the optical losses in the ring are higher than the coupling losses), and when $\alpha <\mid t \mid$ the ring works in the overcoupled regime. Usually, the desired operational point is critical coupling (because the ER reaches its maximum), although operation in the overcoupled regime can have some advantages for long distance transmission because it induces a slightly negative chirp parameter [28].

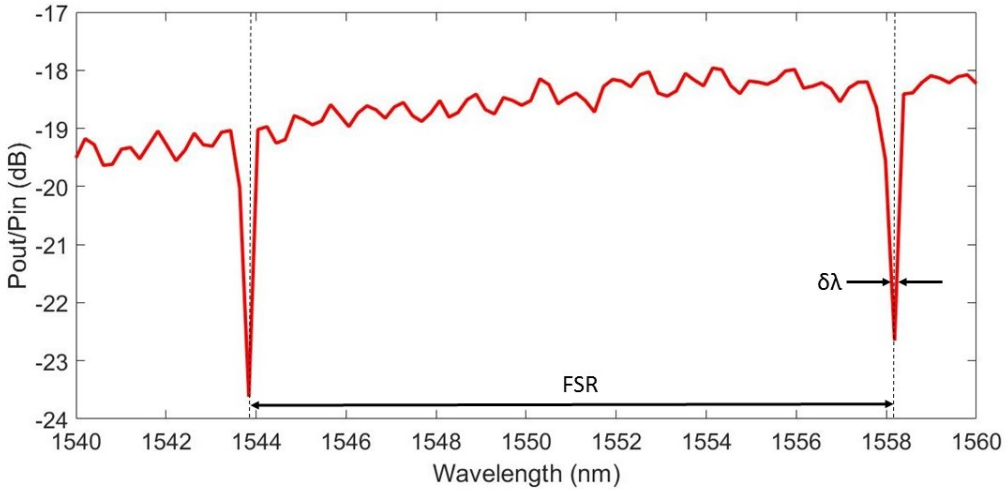

FIGURE 2.3: Experimental transmission spectra of a silicon microring modulator.

A typical microring modulator transmission spectra is shown in figure 2.3. In this figure some important parameters of ring modulators are depicted: the free spectral range (FSR), which is the distance between to consecutive resonances, and the full width half maximum $\delta\lambda$. $\delta\lambda$ is a very important parameter, since it allows to calculate what is known as the quality factor Q of the ring resonance by the relation $Q = \lambda/\delta\lambda$. Q is defined as the ratio between the energy stored by the ring and the energy lost during one round trip and is an important parameter that poses an intrinsic limit to the bandwidth of ring modulators.

Equation 2.6 does also explain how the modulation in ring resonators works: by changing the free carrier density in the ring by applying a voltage, a change in the effective index n_{eff} is induced through the plasma dispersion effect, so the ring undergoes a change in the resonance wavelength λ_r. The change in the resonance wavelength causes the incident light (at a fixed wavelength λ_l) to transition from being in resonance (and having almost zero power at the output, P_0) to being out of resonance (and thus having almost complete transmission at the output, P_1), as depicted in figure 2.4. In this figure another important ring modulator parameter is shown: the modulation efficiency, which measures the amount of change in the resonance wavelength when a voltage is applied and is usually measured in pm/V.

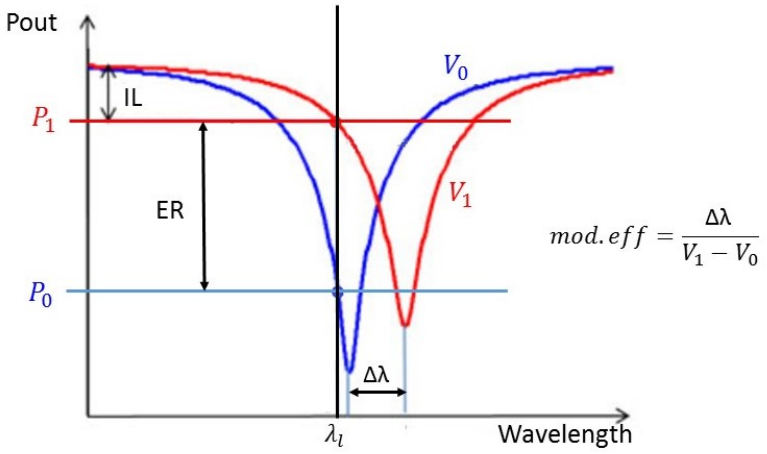

FIGURE 2.4: Working principle of a ring modulator. By applying a voltage, the resonance wavelength of the ring changes (blue and red curves) due to the plasma dispersion effect. As the laser wavelength is fixed at λ_l, the output power is different at each applied voltage (P_1 and P_0). Important parameters of the modulation such as IL and ER are also depicted.

2.3.2 Operation modes and trade-offs

As briefly mentioned before, there are different approaches to generate the necessary change in the free carrier density (FCD) to generate a change in the resonance frequency of the ring through the plasma dispersion effect: carrier depletion and carrier injection. Both of them rely on the use of pn junctions, but while carrier injection operation increases the FCD in the waveguide operating in the forward bias regime (as depicted in Fig 2.1(a)), the carrier depletion approach modulates the width of the depletion region by reverse biasing the junction, decreasing the FCD where the optical mode is confined (Fig 2.1(b)).

Although carrier injection modulators have a higher modulation efficiency because the change in FCD is higher for the same applied voltage compared to the carrier depletion ones, the latter are usually preferred because they can support higher modulation speeds (as they are not intrinsically limited by the minority carrier lifetime in silicon, which is relatively long) and they have better thermal dissipation properties (as the Joule heating is less important in these devices). Because of this reasons, in this thesis carrier depletion ring modulators are discussed and characterized.

Although the purpose of this thesis is not to discuss the design of carrier depletion ring modulators, it is important to have an intuition of the different factors that limit the

performance of these devices. The main trade-off in carrier depletion ring resonators is between ER and BW: carrier depletion modulators' BW is limited by the capacitance (C) and resistance (R) of the device, such that low capacitances are needed for high speed operation. Nevertheless, the ER of the modulator is directly proportional to C (as $ER \propto \Delta n \propto \frac{dQ}{dV} = C$), so some finite capacitance is needed. There is also a trade-off between device footprint and optical losses mainly for two reasons: (1) the ring has to be big enough to prevent the optical mode to be absorbed by the metal contacts positioned inside the ring and (2) the curvature of the ring cannot be infinitely large because then radiation losses would be very high. In the same way, the doping of the p and n regions cannot be too high (which would be good for modulation efficiency), or else the optical losses due to free carrier absorption would be too high. Modal confinement is another aspect to account for when designing ring modulators: the smaller the optical mode, the higher the overlap with the depletion region of the pn junction and the higher the change in the effective index for an applied voltage.

2.4 Silicon modulators: a brief review

In this section, a brief review on the main achievements and efforts carried out by the scientific community in silicon modulators is presented. More comprehensive reviews in this topic can be found in [3] for silicon modulators in general and in [29] and [6] for ring resonator modulators in particular.

Silicon optical modulators have been studied since the mid 1980s [30]. The earliest devices employed carrier injection due to its higher modulation efficiency, and a PIN diode configuration was typically used [26, 31]. These devices were generally slow ($\sim$ MHz), but bandwidths close to the GHz range were achieved by the mid 2000s [32].

The first carrier depletion modulator was proposed in 2005 [33] with a 50 GHz predicted bandwidth, and was realized in 2007 [34], reporting 30 Gbps data transmission.

Ring resonator modulators were introduced in 2005 by Qianfan Xu et al. [5] with the device shown in figure 2.5(a). The carrier injection modulator achieved a data rate of 1.5 Gbps. This rate was increased to 16 Gbps by using pre-emphasis driving signals, a method originally proposed by Png [35] to reduce transition times.

Carrier depletion resonant modulators have been demonstrated with high modulation bandwidth, being 35 GHz [36] the highest bandwidth ever reported for a silicon modulator. Different junction geometries have been explored and reported: vertical [37], horizontal [38] and interdigitated [39] junctions, each one presenting its own advantages and limitations [29]. Figure 2.5(b-d) shows the cross section of these geometries.

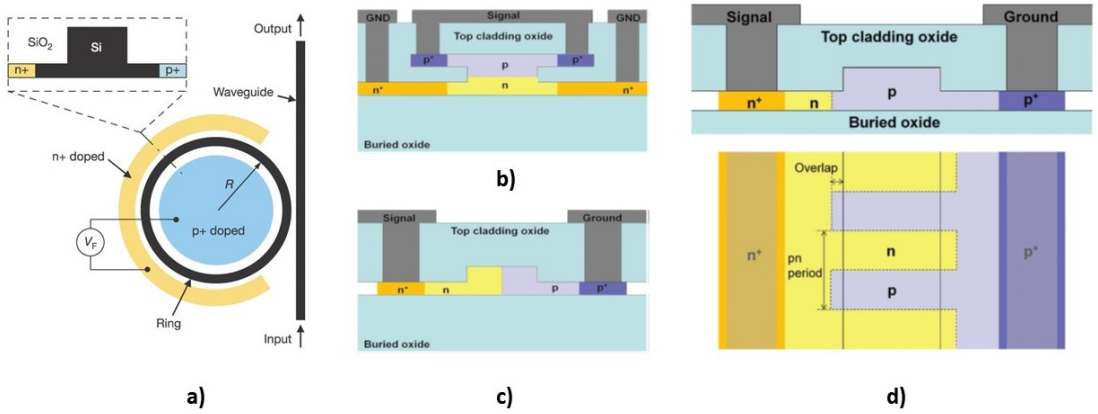

FIGURE 2.5: (a) Geometry of the first silicon ring resonator modulator [5]. (b) Cross section of a vertical pn junction, which runs parallel to the top and bottom surfaces of the waveguide. (c) Cross section of a horizontal (or lateral) pn junction, which runs perpendicular to the top and bottom surfaces of the waveguide. (d) Cross section (top) and plan (bottom) of an interdigitated pn junction. (b), (c) and (d) are taken from [6].

Considerable effort has been made to overcome the limitations of typical resonant modulators using more complex structures such as cascaded dual-ring modulators [40], coupled dual-ring modulators [41], ring-assisted MZI modulators [42], and MZI-coupled ring modulators [43].

All the above-mentioned devices follow monolithic approaches. Hybrid approaches that introduce III-V materials onto the silicon waveguide have also been explored achieving up to 25 Gbps and 10 dB ER [44], as well as SiGe modulators exploiting the Franz-Keldysh effect [45].

2.5 Summary

In this chapter, the basic theory of silicon resonant modulators has been presented.

Performance metrics of optical modulators have been reviewed, and the challenge of obtaining high bandwidth, low loss, low power consumption and high ER modulators has been discussed.

The working principle of silicon resonant modulators has also been reviewed: a change in the FCD of the silicon waveguide generates a change in its effective refractive index through the plasma dispersion effect, which changes the resonance wavelength of the device and switches the device from the on-resonance state (where there's no output light) to the off-resonance state (where the light is transmitted), as depicted in figure 2.4.

Finally, a brief overview of the main achievements accomplished by the research community in silicon modulators has been presented.

Chapter 3

Thin silicon zero-change CMOS microring modulator characterization at 1550 nm

The potential of the zero-change CMOS approach for the design and fabrication of silicon photonics components has been discussed and justified in the first chapter of this thesis: monolithic integration of photonics with electronics enables leveraging the advances of CMOS technology to build large-scale photonic systems and is a promising approach to address the increasing data rate demands.

In this chapter, the high speed characterization of a carrier depletion ring modulator at 1550 nm fabricated in the thin (< 100 nm) silicon device layer in a standard microelectronics SOI CMOS process is presented. Data transmission at 25 Gbps over short distances and 12.5 Gbps over 50 km is demonstrated.

3.1 Modulator geometry

The majority of silicon photonics platforms utilize SOI substrates with a silicon thickness of 200-250 nm [37]. This range is roughly centered at $\lambda/2n_{Si}$ at 1550 nm, and is chosen to guarantee good vertical modal confinement, thus avoiding high radiation losses. Nevertheless, the silicon thickness in the advanced microelectronic SOI CMOS

platforms is one-half to one-third of this range (usually < 100 nm), causing concerns for realizing enough modal confinement for designing compact and efficient devices.

To overcome this limitation the designed device relies on the fundamental whispering gallery mode (WGM) [46] of a 20 μm diameter multimode microring. By exploiting the small modal volume of the zero order WGM, high modal confinement is obtained even for such small silicon thicknesses, keeping the radiation loss of the resonator orders of magnitude below the fabrication-induced scattering loss ($Q_{rad} > 10^9$ vs $Q_{fab} \sim 2 \times 10^4$) [1].

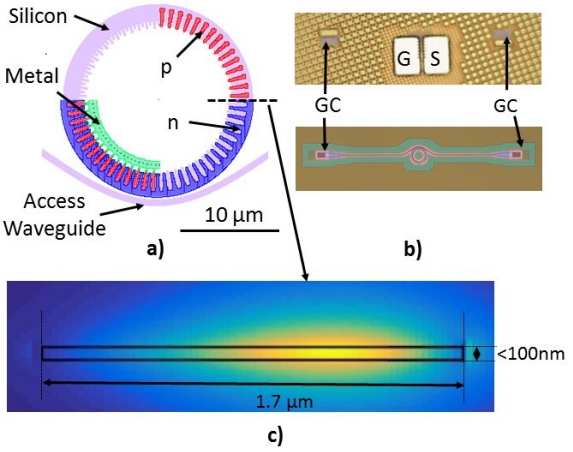

FIGURE 3.1: Modulator geometry. (a) Top view of the 20 μm diameter resonant modulator. Sections of the p and n regions and the metal contacts are shown. (b) Micrograph of the front (top) and back (bottom) of the modulator. Grating couplers (GC), ground (G) and Signal (S) electrodes and optical cavity are recognizeable. (c) Cross section of the WGM profile of the device shown in (a).

The microring device and the profile of the WGM are shown in Fig. 3.1(a,c). The thickness of silicon is less than 100 nm as often found in advanced SOI CMOS processes for the implementation of transistors [2]. The modulator is designed by utilizing the well implants in the CMOS process to realize an interleaved p-n junction around the circumference of the microring (Fig. 3.1(a)). The junctions are optimized for efficient refractive index modulation and high-speed operation in the depletion mode [18], and grating couplers (GC) are used to couple light in and out of the waveguide [47].

[1] Remeber that $Q \propto \frac{Stored\ energy}{Power\ loss}$, so higher Q translates into less losses.

3.2 DC characterization

The DC characterization of the described device was performed using the experimental setup shown in figure 3.2(a). The light coming from an HP8164A tunable laser was coupled into the modulator using a lensed optical fiber, and collected at the output using another lensed fiber. A sweep of the input light wavelength was performed, and the ratio between the input and output light at each of the wavelengths was measured with power meters.

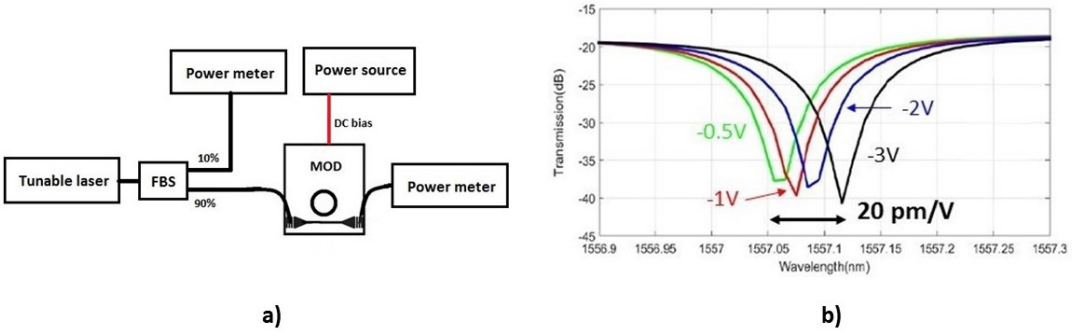

FIGURE 3.2: DC characterization of the ring modulator. (a) Experimental setup showing the electrical (red) and optical (black) paths. Power meters are used to obtain the transmission for each wavelength. FBS = fiber optical beam splitter. (b) Transmission vs wavelength for different bias voltages. The resonance shift is approximately 20 pm/V at -0.5 V bias.

Figure 3.2(b) shows the induced resonance shift of the modulator under an applied DC voltage. As expected, the application of a reverse bias to the modulator red shifts the resonance wavelength of the modulator due to a decrease in the free carrier density (as the width of the depletion region increases with increasing reverse bias). The measured quality factor (Q) is approximately $1.3\text{x}10^4$ and the device exhibits an extinction ratio of $\sim$ 20 dB.

The induced wavelength shift is $\sim$ 20 pm/V at -0.5 V bias, which is twice the modulation efficiency achieved with the 1180 nm modulators fabricated in the same platform [18], and on the same order of magnitude as the efficiencies achieved with non vertical junctions in 200 nm thick silicon, which are around 40 pm/V [48]. The reason is that although the modal confinement is smaller (due to the $<$ 100 nm thickness of the silicon layer), the plasma dispersion effect is enhanced due to higher overlap of the optical mode with the depletion region.

3.3 High speed characterization

The frequency response of the modulator was taken using an Agilent 8722D vector network analyzer (VNA) as depicted in figure 3.3(a). A bias T is used to apply a DC voltage to the device, and the modulated optical signal is converted back to electrical signal by using a commercial high speed photodetector, which is connected to port 2 of the Vector Network Analyzer. To isolate the response of the modulator, the frequency response of the VNA itself is obtained by performing a back to back measurement (connecting port 1 and 2 of the VNA) and subtracted from the measured optical response[2]. For the same reason, the frequency response of the commercial photodetector is also subtracted using the data provided in its datasheet. Figure 3.3(b) shows the experimental optical response of the modulator, with a 3 dB bandwidth of 14 GHz at -2V bias.

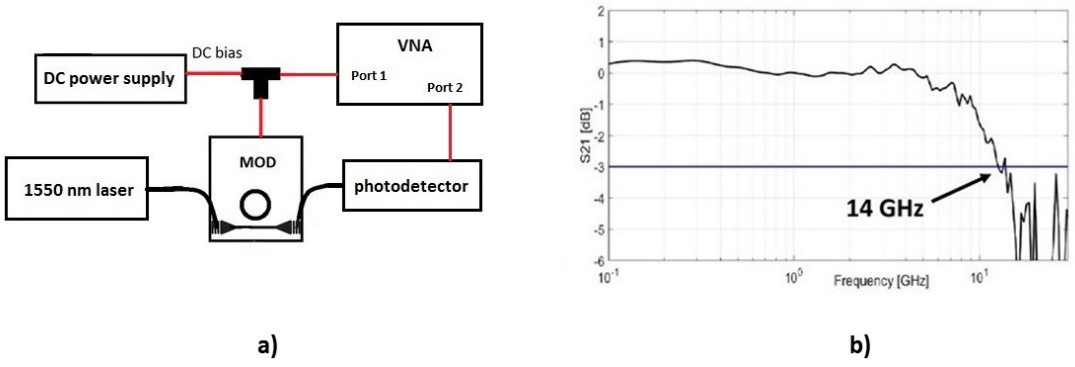

FIGURE 3.3: Modulator bandwidth measurement. (a) Experimental setup showing the electrical (red) and optical (black) paths. A VNA with the driving signal at port 1 and the signal out of a commercial photodetector connected to the modulator at port 2 is used to obtain the frequency response. (b) Small-signal frequency response at -2V bias. The 3dB bandwidth is around 14GHz.

The performed bandwidth measurements confirm the suitability of the modulator to sustain high data rate transmission. Eye diagrams of the resulting modulated signal were taken using the experimental setup depicted in figure 3.4. The modulator was driven by an electrical signal coming out of Picosecond Pulse Labs 12072 32 Gbps pattern generator. A RF amplifier is used to adjust the amplitude of the driving signal to the desired value. To compensate for the $\sim$ 20 dB losses introduced by the non-optimized grating couplers, the output light of the modulator is amplified using an Erbium Doped Fiber Amplifier (EDFA) followed by an Amplified Spontaneous Emission (ASE) rejection filter. The modulated and amplified light is converted back to electrical signal using a

[2] Appendix B contains the matlab codes that perform this subtraction and obtain the bandwidth of the device form the VNA data.

commercial high speed photodetector, and an Agilent DCA-X 86100D high bandwidth oscilloscope is used to monitor the generated signal.

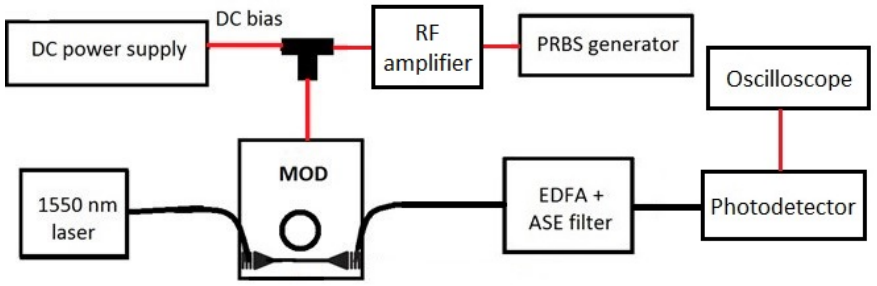

FIGURE 3.4: Experimental setup showing the electrical (red) and optical (black) paths for the acquisition of eye diagrams.

Figure 3.5 shows the obtained eye diagrams for different modulation rates and driving voltages. In all cases the bias voltage was set at -2 V and the driving signal was a $2^{11}-1$ pseudo random binary sequence (PRBS). The device is approximated as an open circuit, so the amplitude of the driving voltage is calculated assuming voltage doubling at the open terminals. For example, if the driving signal has 0.8 V_{pp} at the output of the RF amplifier, a 1.6 V_{pp} amplitude is assumed at the device terminals.

2.19 dB ER and a small IL of 0.26 dB were achieved at 25 Gbps with a 1.6 V_{pp} driving voltage on device terminals and 2 V reverse bias as shown in Figure 3.5(a). Note that this drive voltage is compatible with the CMOS technology that this device was built in, demonstrating the possibility of implementing monolithic high-speed transmitters at 1550 nm using thin silicon devices.

Figure 3.5(b) shows a 6.23 dB ER and 0.5 dB IL at 25 Gbps with a 3.6 V_{pp} driving voltage. 3.24 dB ER and 0.2 dB IL modulation at 32 Gbps using 3.6 V_{pp} driving voltage was also achieved, as demonstrated in figure 3.5(c).

3.4 Transmission over moderate distances

Silicon modulators are usually considered for short-reach communication links. Therefore, the study of device characteristics that are important as link distances are increased (i.e. the chirp parameter) is often ignored. As the bandwidth of silicon modulators has

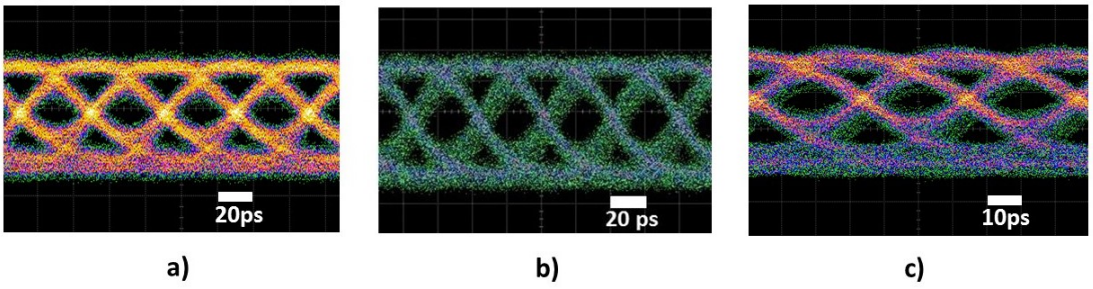

FIGURE 3.5: Eye diagrams for different data rates and driving voltages. (a) 2.10 dB ER and 0.26 dB IL eye at 25 Gbps and 1.6 V_{pp}. (b) 6.23 dB ER and 0.5 dB IL eye at 25 Gbps and 3.6 V_{pp}. (c) 3.24 dB ER and 0.2 dB IL eye at 32 Gbps and 3.6 V_{pp}.

dramatically improved, applications for moderate-reach, dispersion uncompensated systems (up to 100 km) has begun to receive attention [49, 50]. It is interesting then to evaluate the suitability of the characterized modulator for such applications.

3.4.1 Chirp parameter

In general, to evaluate the feasibility of using a modulator for moderate distance, dispersion-uncompensated applications it is necessary to characterize the chirp parameter of the modulated signal that comes out of the modulator.

The chirp parameter α in small signal conditions is defined as [51]:

$$\alpha = -2I(V)\frac{d\phi(V)}{dI(V)} \tag{3.1}$$

Where $I(V)$ and $\phi(V)$ are the optical intensity and phase of the output signal, which depend on the voltage applied to the modulator. In short, the chirp parameter of a signal is 0 when a change in its intensity is not accompanied by a change in its phase, and is different from 0 otherwise.

The evaluation of the chirp parameter is important because it sets an upper limit to the maximum distance an optical signal can travel over a SMF without suffering fatal intersymbol interference (ISI) due to the chromatic dispersion of SMF [52]: a positive chirped signal will suffer pulse broadening, therefore causing ISI and deteriorating the system performance.

In fact, it is possible to evaluate the maximum distance an optical signal can travel over a SMF at a given data rate with the following equation [52]:

$$B^2 L_{max} = \frac{c}{2D\lambda^2}(1 - \frac{2}{\pi} arctan(\alpha)) \tag{3.2}$$

Where B is the data rate of the modulation, L_{max} is the maximum distance the signal can travel before suffering fatal ISI, D is the dispersion of the fiber over which the signal propagates and λ is the wavelength of the laser carrying the modulated signal.

From equation 3.2 it is clear that, for propagation over standard single-mode fiber at 1550 nm wavelength (with a dispersion $D \sim 20ps/(nm * km)$), a small negative chirp is beneficial.

Microring resonant modulators are inherently dispersive (that is, they induce non-zero chirp to the modulated signal) because of the non-zero phase response of their transfer function[3] [28]. Moreover, the chirp parameter depends strongly on the modulation conditions, such as bias voltage, input power and detuning between the laser wavelength and the resonance wavelength of the modulator (i.e, the difference $W_0 - W_l$), because all this parameters change this transfer function.

Here, a characterization of the small signal chirp parameter induced by the modulator for different bias voltages and detunings of the laser wavelength with respect to the resonance wavelength is performed using the method presented in [53]. Figure 3.6(a) shows the experimental setup used for this purpose, in which a dispersive media (in this case a 50 km SMF) is used to generate interference between the carrier frequency component of the signal and the two first order sidebands that appear as a result of the modulation[4]. By looking at the frequencies in which destructive interference occurs with the use of a VNA, the chirp parameter and fiber dispersion can be extracted[5].

Figure 3.6(b) shows the results. When operated at the blue side of the resonance ($\lambda_l - \lambda_0 < 0$) the microring induces a negative chirp, and the magnitude of the chirp decreases as the reverse bias voltage decreases. These results match well with the theoretical analysis in [28].

[3] See appendix A for the derivation of the transfer function of resonant modulators

[4] The theoretical derivation of the method is comprehensively described in [53].

[5] Appendix C contains the matlab codes that obtain both chirp parameter and dispersion from the VNA data.

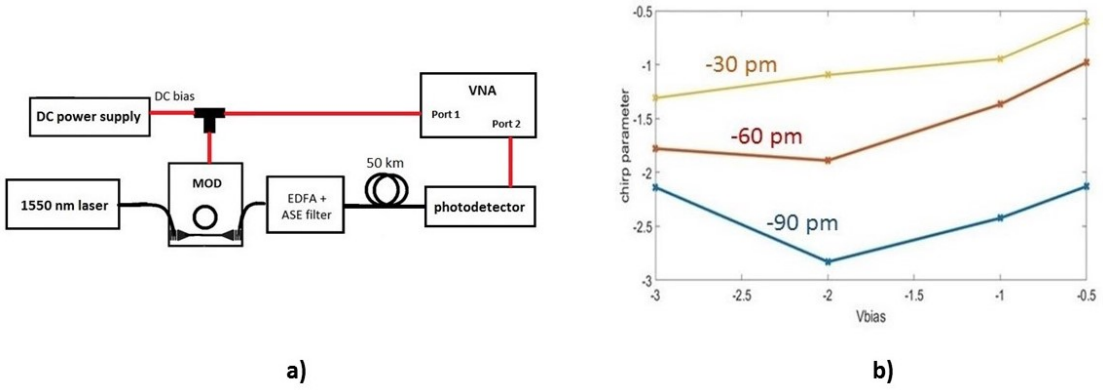

FIGURE 3.6: Chirp characterization. (a) Experimental setup showing the electrical (red) and optical (black) paths. (b) Chirp parameter vs bias voltage. Different curves show different detunings from the resonance wavelength of the resonator.

As already discussed in equation 3.2, a slightly negative chirp is beneficial for long distance transmission, as it compensates for the chromatic dispersion of single mode fibers. The resulting maximum B^2L for transmission over a standard single mode fiber at 1550 nm with the measured negative chirp is around 6000 $Gbps^2 \cdot km$, 66% higher than the 3600 $Gbps^2 \cdot km$ limit with zero chirp. This means, for example, that $L_{max-chirp} = 38.4\ km$ for a 12.5 Gbps signal modulated with the characterized device, compared to $L_{max-no-chirp} = 23\ km$ for a signal with no chirp.

It can be concluded, then, that the modulator is suitable for moderate distance, dispersion uncompensated communication systems.

Nevertheless, a caveat should be added here. Although the definition of chirp parameter is clear from a theoretical point of view, it is difficult to evaluate it experimentally, mainly because it has a non-trivial dependence with time [54]. Not only this, but this time dependence makes difficult to relate the (time-dependent) chirp parameter to its effects on the transmission over SMF. To the best of the author's knowledge, a thorough discussion about the time dependence of the chirp parameter induced by resonant modulators and its effects over propagation is yet to be done. Nevertheless, some effort has been done to provide definitions of an "effective" chirp parameter that is independent of time and is suitable for the evaluation of long distance transmission, such as on-off chirp parameter or 3 dB chirp parameter [55]. The downside of these definitions is that they are difficult to measure, so their usage has been limited to theoretical analysis.

3.4.2 Eye diagrams

The small signal chirp parameter analysis concludes that the negative chirp induced by the modulator benefits moderate distance transmission. Nevertheless, the amplitude of the driving electrical signal necessary to achieve a good enough ER modulation is too large to consider the small signal approximation as correct. It is necessary, then, to further explore the quality of the modulated signal after moderate (50 - 75 Km) distance transmission when the amplitude of the driving signal is large.

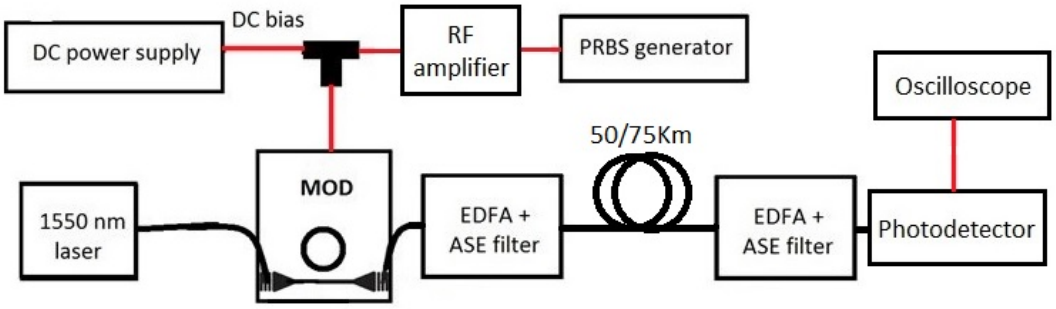

FIGURE 3.7: Experimental setup for the acquisition of eye diagrams after propagation over SMF.

To do so, the experimental setup depicted in figure 3.7 is used. Note that this is the same setup used for the high speed modulation characterization, with a variable length single mode optical fiber (SMF) spool added between the EDFA and the photodetector. A second EDFA and ASE filter block is used to compensate for the losses due to the propagation of the signal through the SMF (which adds a loss of ~ 0.2 dB/km).

Figure 3.8 shows the recorded eye diagrams for a 12.5 Gbps signal transmitted over 50 and 75 km of fiber. The effect of the dispersion is clearly visible as a distortion and widening of the pulse. Nevertheless, the eye is still open, demonstrating the potential of the device for moderate distance data transmission.

3.5 Optical link

The modulator characteristics described above suggest the possibility to build a high data rate, moderate distance transmission link at 1550 nm using the thin silicon zero change CMOS platform presented here.

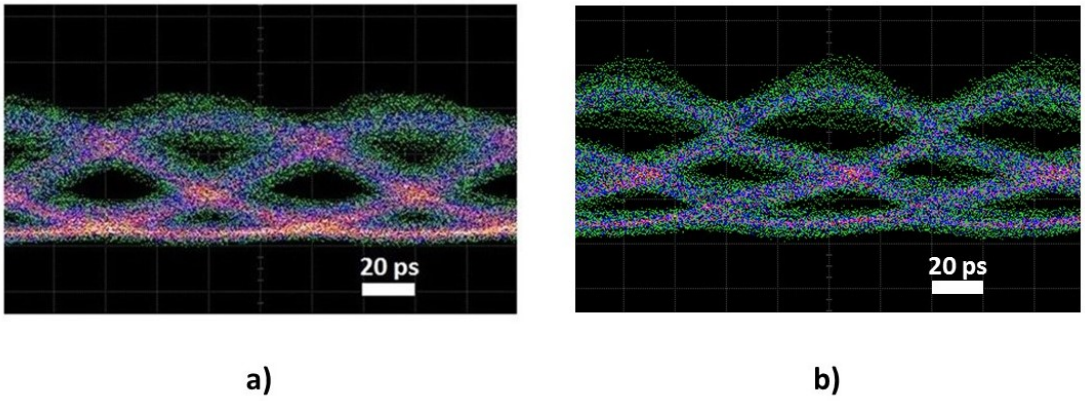

FIGURE 3.8: 12.5 Gbps eye diagrams after moderate distance propagation. A 1.6 V_{pp}, $2^{11} - 1$ PRBS driving signal and 2 V reverse bias are used. (a) Recorded eye diagram after 50 km propagation over SMF. (b) Recorded eye diagram after 75 km propagation over SMF.

To further explore this option, an optical link was built using the resonant modulator characterized here and a polysilicon photodetector fabricated in the same thin silicon platform with the zero change CMOS approach [19]. The 3 dB bandwidth of the detector is 10 GHz at 15 V bias with 0.15 A/W responsivity at 1550 nm.

Figure 3.9(a) shows the experimental setup for the link measurement. The modulator was driven by a 3.6 V_{pp} $2^{11} - 1$ PRBS signal. An EDFA was used to compensate the 30 dB losses introduced by the unoptimized grating couplers ($\sim$ 20 dB at the modulator and $\sim$ 10 dB at the detector). A bias T was used to apply 20 V reverse bias to the photodetector, and the AC port of the same bias T was connected to a high speed oscilloscope to record the electrical signal generated by the photodetector.

As the resonance wavelengths of the modulator and the detector do not match exactly due to fabrication tolerances, an LFI-3751 temperature controller was used to manually thermally tune the resonance wavelength of the modulator exploiting silicon's thermooptic effect.

Figure 3.9(b) shows the obtained eye diagram at 15 Gbps data rate. Although the high losses introduced by the couplers did not allow to perform BER tests, this is the first proof of the feasibility to build a fully resonant optical link at 1550 nm wavelength in a microelectronics CMOS platform with a thin silicon device layer. To the best of the author's knowledge, this is the first ever demonstrated resonant modulator - resonant detector silicon photonics optical link.

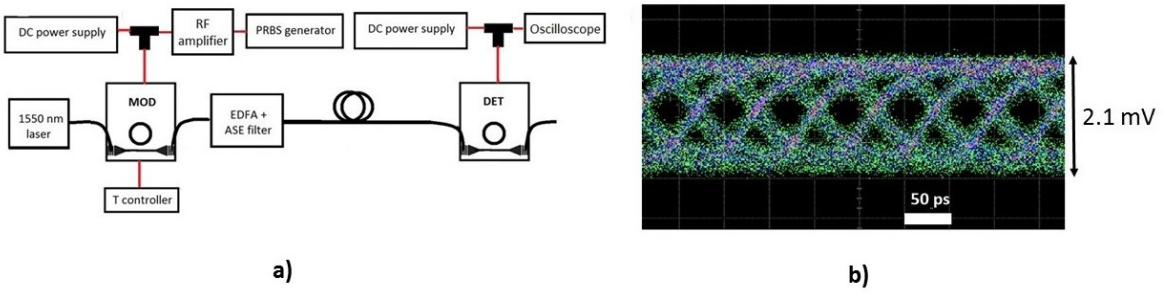

FIGURE 3.9: Link measurement. (a) Experimental setup for the link measurement showing the electrical (red) and optical (black) paths. (b) 15 Gbps eye diagram. The modulator driving voltage is 3.6 V_{pp} at -2 V bias, while the detector is biased at 20 V.

As will be discussed later in chapter 4 of this thesis, nonlinearities that arise due to the high power density buildup that takes place in ring resonators change the resonance wavelength of these devices. The dominating effects are local changes in the temperature of the resonators, which have been demonstrated to have a huge impact in the quality of the eye and the error performance of the devices [56], so thermal stabilization of the resonances would allow for a better quality of the link. It is worth mentioning that this assertion is not only valid for the optical link, but is also valid for the modulator operation that has been characterized in the previous sections. It follows, then, that better performance of both the modulator itself and the optical link could be obtained at the expense of power consumption and complexity by integrating resonance thermal stabilization circuits, as shown in [56].

3.6 Conclusion

In this chapter the challenges faced in implementing efficient and high bandwidth (>10 GHz) modulators at telecommunication wavelengths in a thin body silicon layer (<100 nm, which is preferred for transistor performance in monolithic electronic-photonic platforms) have been addressed.

A resonant modulator that is designed to avoid strong radiation losses at 1550 nm in thin silicon layers has been presented and characterized. The carrier depletion based modulator has a 14 GHz 3dB bandwidth and enables 25 Gbps and 12.5 Gbps data transmission over short (∼1m) and moderate (50 km) distances, respectively.

A detailed study of the chirp characteristics of this device has been performed to investigate its potential for communication over long distances. Slightly negative chirp parameter is measured, which is beneficial for long distance transmission.

A complete optical link at 15 Gbps using the studied modulator and a polysilicon detector fabricated in the same platform has also been demonstrated, showing the potential to build small-footprint, high-speed and large-scale systems for telecommunications in standard microelectronics CMOS.

By realizing high-speed and efficient optical modulators at the telecommunications wavelength in thin silicon layers utilized in the microelectronics industry, the potential of these CMOS photonic platforms for addressing the future demands in telecom and datacom systems has been unveiled. At a broader scale, realization of high performance photonic devices in microelectronic CMOS platforms without any change to the process flow opens up new opportunities for building large scale electronic-photonic chip-scale systems for a wide range of applications in communications, computation, and signal processing.

Chapter 4

Nonlinearities in microring modulators

The amount of optical power at the output of a resonant modulator is, of course, dependent on the amount of power at its input. It then follows that, to avoid the use of optical amplifiers at the output of the modulator (thus decreasing the complexity, noise and power consumption of the transmitter system) and still have enough signal power for successful transmission it is desirable to use as much optical power as possible at the input of the modulator.

Nevertheless, the strong light confinement and electric field enhancement that microring modulators achieve due to its resonant nature gives rise to high power densities, which combined with the fact that silicon exhibits high third-order nonlinearity [57], generate nonlinear effects that can cause unexpected behaviors even for low input powers. As the input power in the resonator increases, so does the strength of these nonlinear effects, which affect the performance of the modulator.

In fact, both thermal [58] and carrier [59] induced optical bistability have been reported in silicon ring resonators, and self-pulsation due to the competition between both processes has also been observed [60].

The necessity of a tool to model the behavior of these nonlinearities and its effects in the modulator performance is thus clear, as it provides valuable insight into the physical

processes that play a role in resonant modulators and, ultimately, a way to evaluate the power handling capabilities of resonant modulators.

In this chapter, the derivation of such a model and its application to the silicon microring modulator described in chapter 3 is addressed. The power handling capabilities of silicon resonant modulators are also discussed using the derived model.

4.1 Relevant nonlinear effects in silicon resonant modulators

Silicon shows a wealth of nonlinear effects [61], but here we will only focus on the nonlinear effects dominant in resonant modulators. References [61, 62] are a good review for nonlinearities in silicon and its applications[1] .

There are two main nonlinear effects that play a role in the behavior of silicon resonant modulators: two photon absorption (TPA) and thermal effects.

TPA is the process by which an electron-hole pair is generated by the simultaneous absorption of two photons, and it has a quadratic dependence with the energy stored in the microring. The TPA process generates additional free carriers in the waveguide, which change the resonance wavelength of the ring modulator (through the plasma dispersion effect) and also generate local heating of the waveguide due to increased free carrier absorption (FCA). FCA is the process in which a carrier is excited from an already-excited state to another through the absorption of a photon. The non-radiative relaxation of the excited carrier generates phonons, which translates into a self-heating of the waveguide.

Thermal effects due to local changes in the temperature of the silicon waveguide that carries the propagating optical mode do also change the resonance wavelength of the modulator, as the effective index of refraction depends highly on the waveguide temperature [25].

[1] Although nonlinear behavior is generally not desired for resonant modulation, which is the focus of this thesis, a lot of interesting applications have been reported in the literature that exploit nonlinearities in silicon waveguides, such as amplification [63], cross-phase and cross-amplitude modulation [64], switching [65] and wavelength conversion [66].

The dependencies between these two effects are non trivial, and the reason for this is that, as will be discussed later in detail, the two effects move the resonance in the opposite direction: an increase in the number of free carriers due to TPA generates a blue shift of the resonance (that is, decreases the resonance wavelength), whereas an increase in the temperature red shifts the resonance (that is, increases the resonance wavelength). The fact that the time scales of these two effects are also very different (TPA is an instantaneous process, but heating has a time constant in the order of μs) adds more complexity to the nonlinear behavior of silicon resonant modulators.

The change in the resonance wavelength generated by these two effects is, in general, not desired, since ideally the only variable controlling the resonance wavelength (and, therefore, the '0' and '1' power levels and the transition between them) should be the applied voltage. It is then clear that a limitation in the input power on the modulator should exist, such that the effects of these nonlinearities do not affect in a relevant manner the modulator's performance.

4.2 Model derivation

A model to describe nonlinearities that occur in high Q silicon resonant microdisks has already been derived by Painter [60]. We will follow closely the derivation in [60], and the model will be extended to include the effect of an active modulation of the resonance wavelength by an applied voltage.

The amplitude of the optical mode travelling along a ring resonator coupled to an input waveguide can be derived using the coupling of modes in time formulism, considering the ring as a lumped oscillator with resonance frequency W_0 and an amplitude decay constant $\gamma/2$ [21, 67], yielding the following equations:

$$\frac{da}{dt} = (-\frac{\gamma}{2} + j\Delta W_0)\ a - j\kappa s_{in} \tag{4.1}$$

$$s_{out} = s_{in} - j\kappa^* a \tag{4.2}$$

where κ is the coefficient of coupling between the ring and the waveguide, $\Delta W_0 = W_0 - W_l$ is the detuning between the wavelength of the input light and the resonance wavelength of the modulator, $|s_{in}|^2$ is the input power into the modulator and $|s_{out}|^2$ is the power at the output of the modulator. The mode amplitude a is defined such that the energy stored in the ring is $U = |a|^2$.

Note that here, as opposed to [60], the splitting of the cosine- and sine-like degenerate modes is not considered, as these is only observed in high-Q ($> 10^5$) resonant structures, which is not the case for the modulators studied in this thesis.

4.2.1 Loss rate

The loss rate γ defined above can be mapped to more familiar parameters of the resonator. In fact $\gamma = 1/\tau$, where τ is the decay time constant of the power inside the resonator. Using the fact that $Q = W_0\tau$, γ and Q can be directly related by $Q = W_0/\gamma$.

The mode's loss rate γ can be separated in different terms, corresponding to different loss mechanisms:

$$\gamma = \gamma_0 + \gamma_{rad} + \gamma_{background} + \gamma_{TPA} + \gamma_{FCA} \tag{4.3}$$

where γ_0 are the losses due to the coupling between the ring and the bus waveguide, γ_{rad} are the losses due to radiation and scattering in the ring, $\gamma_{background}$ are the losses due to the free carrier population generated by the thermal ionization of acceptor and donor impurities and γ_{TPA} and γ_{FCA} are losses due to TPA and FCA respectively. By power conservation, $\kappa = \sqrt{\gamma_0}$ [67]. Note here the assumption that there are no losses due to coupling to higher order modes of the ring.

While γ_0, γ_{rad} and γ_{back} are constant parameters of the ring, γ_{TPA} and γ_{FCA} depend on the density of free carriers in the ring which, in turn, depend on the amount of energy stored in it.

It is important to note that the optical mode does not have a uniform electric field distribution in a cross section of the ring waveguide, as shown in figure 3.1 for the modulator characterized in chapter 3. It is then necessary to account for this non-uniformity in this model, since it is clear that TPA will occur mainly in the areas where

the optical mode is more intense. To do so, we follow the approach in [68], which consists in introducing weighted averages of the local rates at each position in the waveguide for the specific propagating optical mode. With this, we can define [68]:

$$\gamma_{TPA}(t) = \Gamma_{TPA}\frac{\beta_{Si}c^2}{V_{TPA}n_g^2}U(t) \tag{4.4}$$

Where c is the speed of light in vacuum, n_g is the group index of the optical mode, β_{Si} is the intensity loss per unit length due to TPA and Γ_{TPA} and V_{TPA} account for the non uniformity of the mode and are defined as:

$$\Gamma_{TPA} = \frac{\int_{Si}|E(\mathbf{r})|^4 d\mathbf{r}}{\int n^4(\mathbf{r})|E(\mathbf{r})|^4 d\mathbf{r}} \tag{4.5}$$

$$V_{TPA} = \frac{\left(\frac{1}{n_{Si}\epsilon_0 c}\right)^2 \left(\int Re\{\mathbf{E}(\mathbf{r}) \wedge \mathbf{H}^*(\mathbf{r})\}\hat{e_z}d\mathbf{r}\right)^2}{\int n^4(\mathbf{r})|E(\mathbf{r})|^4 d\mathbf{r}} \tag{4.6}$$

Note that the definitions of the mode averaged parameters are different than the ones used in [60] to account for the high index contrast achieved in these type of devices[69].

As already discussed, the generation of carriers due to TPA generates additional optical losses due to FCA, which can be written as:

$$\gamma_{FCA}(t) = \frac{(\alpha_p + \alpha_n)c}{n_g}\overline{N(t)} \tag{4.7}$$

where α_p and α_n are the loss coefficients given by the Soref's equation presented in chapter 2 (see equation 2.2).

Note that we are not considering the free carrier population due to ionized acceptors and donors. As this population is not time dependent (since at room temperature all the impurities are ionized due to thermal energy), the associated optical losses are constant and can be considered as a background loss included in γ_{back}.

In equation 4.7, we again account for the non-uniformity of the electric field distribution by defining:

$$\overline{N(t)} = \frac{\int N(\mathbf{r},t)n^2(\mathbf{r})|E(\mathbf{r})|^2 d\mathbf{r}}{\int n^2(\mathbf{r})|E(\mathbf{r})|^2 d\mathbf{r}} \tag{4.8}$$

With the above definitions we can then obtain the total power absorbed in the ring at a given time:

$$P_{abs}(t) = (\gamma_{back} + \gamma_{TPA} + \gamma_{FCA})U(t) \tag{4.9}$$

4.2.2 Microring resonance wavelength

As discussed, both the generated free carriers (through the plasma dispersion effect) and the induced self-heating of the waveguide (through thermal dispersion) induce a change in the resonance wavelength of the ring.

From equation 2.6 and the identity $\Delta\lambda = -\Delta f \cdot c/f^2$ the relationship between a change in the refractive index of the waveguide Δn and the induced change in the resonance wavelength ΔW_0 is immediate:

$$\frac{\Delta W_0(t)}{W_0} = -\frac{\overline{\Delta n(t)}}{n} \tag{4.10}$$

where, again, we account for the non-uniformity of the field distribution by mode-averaging:

$$\frac{\overline{\Delta n(t)}}{n} = \frac{\int \frac{\Delta n(\mathbf{r},t)}{n(\mathbf{r})} n^2(\mathbf{r})|E(\mathbf{r})|^2 d\mathbf{r}}{\int n^2(\mathbf{r})|E(\mathbf{r})|^2 d\mathbf{r}} \tag{4.11}$$

Noticing that the change in the refractive index Δn is due to thermal and free carrier dispersion and using equation 4.10 we can write:

$$\frac{\Delta W_0(t)}{W_0} = -\frac{1}{n_{Si}} \left(\frac{dn_{Si}}{dT} \overline{\Delta T(t)} + \left(\frac{dn_{Si}}{dN_p} + \frac{dn_{Si}}{dN_n} \right) \overline{N(t)} \right) \tag{4.12}$$

where $\frac{dn_{Si}}{dT}$ is the thermo-optic coefficient of silicon, $\frac{dn_{Si}}{dN_n}$ and $\frac{dn_{Si}}{dN_p}$ are the free carrier dispersion coefficient for electrons and holes respectively (which can be directly obtained

from Soref's equation 2.1), n_{Si} is the refractive index of silicon, $\overline{\Delta T(t)}$ the mode-averaged temperature difference between the silicon waveguide and the environment and $\overline{N(t)}$ is defined as in equation 4.8 to, again, account for the non-uniformity of the mode profile.

Equation 4.12 is valid in the absence of modulation, i.e, in the absence of an applied time varying voltage to the pn junctions that constitute the ring. To account for the effect of the modulation, a new term has to be added:

$$\frac{\Delta W_0(t)}{W_0} = -\frac{1}{n_{Si}}\left(\frac{dn_{Si}}{dT}\overline{\Delta T(t)} + \left(\frac{dn_{Si}}{dN_p} + \frac{dn_{Si}}{dN_n}\right)\overline{N(t)}\right) + \frac{\Delta W_{0_{mod}}(t)}{W_0} \tag{4.13}$$

This additional term $\Delta W_{0_{mod}}$ is, of course, dependent on the voltage applied to the modulator as well as the dynamics of the pn-junction. The dynamic behavior of the system will be discussed in the next subsection.

Note the important simplification made when adding modulation. Strictly, the effect of the modulation of the depletion region width should be translated into a change in the free carrier density distribution, which would then translate to a change in the resonance wavelength and in the loss rates through the equations derived above. This would, nevertheless, add a lot of complexity to the model, since the geometry and layout of the microring should be included, the depletion region width derived for each applied voltage and the mode averages recalculated at each time step. Instead, for the sake of simplicity we reduce the effect of the modulation to an additional term affecting the resonance wavelength, and no effect in the loss rates is included. This is, at a first order, a valid assumption, since the depletion region width change due to the modulation is in the order of 10 nm (this can be calculated assuming a simple 1 dimensional pn junction [20]) for the usual range of doping levels, which is small compared to the $\sim 1\mu m$ width of the optical mode.

4.2.3 Dynamic equations

To complete the model, the dependence of all the relevant variables of the system with time has to be introduced.

Let's start by the time dependence of the voltage through the pn junction. When a voltage is applied to the device electrodes, a finite time is needed to pull the charges

out of the depletion region or inject charges into the depletion region, that is, there's an associated time constant for the process of modulating the depletion region width. This time constant is dictated by the resistance R and the capacitance C of the depletion region, which are themselves depend on the applied voltage so, ultimately, dependent on time [70]. Assuming that the depletion region modulation is a first order system with a time-varying time constant $\tau(t) = 1/(R(t) * C(t))$, we can write:

$$\frac{dV_{pn}(t)}{dt} = -\frac{V_{pn}(t)}{\tau(V_{pn}(t))} + V(t) \tag{4.14}$$

The calculation of the dependence of τ with the applied voltage is not trivial, and it has to account for the specific geometry of the modulator being simulated. While for simple geometries this dependence can be obtained analytically (for instance, for a 1D pn junction), for complex geometries the use of semiconductor physics simulators such as Sentaurus [71] is necessary.

The voltage through the pn junction can be directly related to the shift in the resonance frequency due to the modulation:

$$\Delta W_{0_{mod}}(t) = \frac{dW_0}{dV} V_{pn}(t) \tag{4.15}$$

where dW_0/dV is a parameter modeling the wavelength shift due to an applied voltage.

The time evolution of the temperature can be also derived from energy conservation principles [72]:

$$\frac{d\overline{\Delta T(t)}}{dt} = -\gamma_{th}\overline{\Delta T(t)} + \frac{\Gamma_{disk}}{\rho_{Si} c_{p,Si} V_{ring}} P_{abs}(t) \tag{4.16}$$

Several assumptions are made here. First, radiation and convection are disregarded. Second, as silicon has a high thermal conductivity, we consider that the temperature is uniform all over the waveguide ($\Delta T(\mathbf{r}, t) = \Delta T(t)$). Finally, we assume that the power dissipation is instantaneous, that is, the heating at time t depends on the absorbed power P_{abs} at that same time t.

The non-uniformity of the mode profile is again considered by defining:

$$\Gamma_{disk} = \frac{\int_{Si} |E(\mathbf{r})|^2 d\mathbf{r}}{\left(\frac{1}{n_{Si}\epsilon_0 c}\right) \int Re\{\mathbf{E}(\mathbf{r}) \wedge \mathbf{H}^*(\mathbf{r})\} \hat{e_z} d\mathbf{r}} \tag{4.17}$$

For free carrier population, two mechanisms are relevant: recombination processes that decrease the free carrier density and TPA, which generates carriers. Performing again a mode average, we can thus write:

$$\frac{d\overline{N(t)}}{dt} = -\gamma_{fc}\overline{N(t)} + \overline{G(t)} \tag{4.18}$$

where $\overline{G(t)}$ is the rate of free carrier generation due to TPA and γ_{fc} accounts for all the processes that reduce the population of free carriers where the optical mode is confined. These are mainly carrier recombination (which include a variety of processes such as non-radiative recombination, Auger recombination...), drift (due to the applied voltage, the generated free carriers are swept away from the center of the waveguide, which is where the optical mode is concentrated) and diffusion due to carrier density gradients along the waveguide.

Again, in the definition of equation 4.18 several approximations have been made. First of all, the recombination rate γ_{fc} is, in principle, dependent on the position. Here, we consider an "average" recombination rate that is uniform all over the waveguide. Note also that no diffusion or drift terms are present. Instead, both processes are included in the decay rate γ_{fc}, which simplifies the model.

The generation rate G is easy to derive, as for every two photons absorbed one electron-hole pair is generated [68]:

$$\overline{G(t)} = \frac{\Gamma_{FCA}\beta_{Si}c^2}{2\hbar W_l n_g^2 V_{FCA}^2} U(t)^2 \tag{4.19}$$

where we define the mode averages:

$$\Gamma_{FCA} = \frac{\int_{Si} |E(\mathbf{r})|^6 d\mathbf{r}}{\int n^6(\mathbf{r}) |E(\mathbf{r})|^6 d\mathbf{r}} \tag{4.20}$$

$$V_{FCA}^2 = \frac{\left(\frac{1}{n_{Si}\epsilon_0 c}\right)^3 \left(\int Re\{\mathbf{E}(\mathbf{r}) \wedge \mathbf{H}^*(\mathbf{r})\}\hat{e_z}d\mathbf{r}\right)^3}{\int_{Si} n^6(\mathbf{r})|E(\mathbf{r})|^6 d\mathbf{r}} \tag{4.21}$$

With this, the derivation of the model is completed. Equations 4.1, 4.13, 4.14, 4.16 and 4.18 constitute the core of the model.

Note that the model presented uses a lot of parameters that need to be accurate if meaningful results are to be obtained. While some of them are general parameters well-known from the literature, some others are specific for the geometry or device to be tested. The way to derive (experimentally or by simulation) these parameters is described in appendix B, and the method is used to obtain the parameters for the device characterized in chapter 3 which, unless otherwise stated, will be the parameters used for the simulations presented in this chapter.

4.3 A simple case

Before simulating the actual modulation of the ring, it is worth analyzing a simpler case in which there's no applied voltage so we can get a good understanding of the different nonlinear processes involved.

To do so, the derived model is simulated setting the drive voltage $V(t) = 0$, which is equivalent to say that the ring is not being modulated. Figure 4.1 shows the simulated temporal behavior of the relevant variables of the system for $\lambda_0 = 1567.2nm, \lambda_l = 1567.1nm$ and $P_{in} = 5mW$ [2].

For such a high input power, self modulation of the ring transmission over time is obtained, a behavior that has been experimentally observed and modeled [60].

Figure 4.1 shines light into the reason of this behavior. Four different time domains can be distinguished at each cycle.

(1) First (times 0 to 25 ns), a rapid build up of free carrier population due to TPA happens due to the combined fact that there's a high input power getting into the resonator and the fact that the laser wavelength and the resonance wavelength are very

[2] A variable-step, variable-order (VSVO) Adams-Bashforth-Moulton PECE (Predict, Evaluate, Correct, Evaluate) solver is used to simulate numerically the system, using 0 initial conditions.

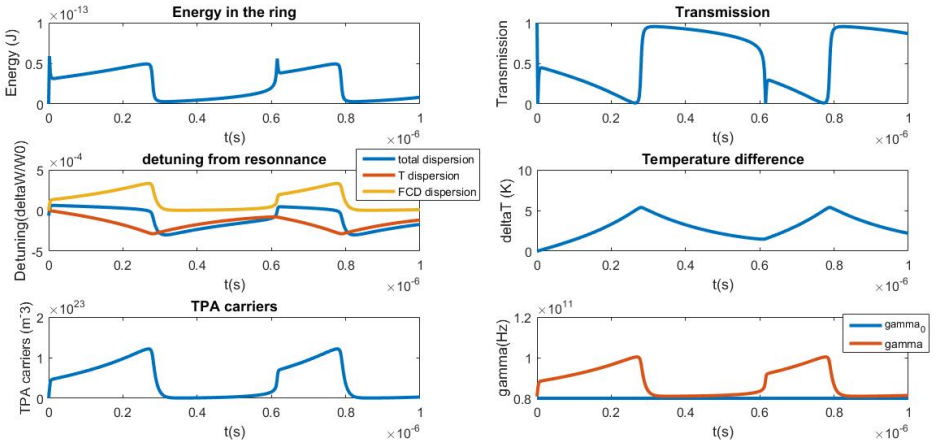

FIGURE 4.1: System temporal behavior for $\lambda_0 = 1567.2\ nm, \lambda_l = 1567.1\ nm$, $P_{in} = 5\ mW$ and no modulation. Self modulation is observed.

close. Two major consequences arise from that: one, the energy in the ring experiences also a rapid rise and two, the dispersion due to the generated free carriers causes a blue shift in the resonance wavelength, which eventually crosses the laser wavelength (as can be seen in the "detuning from resonance graph" of figure 4.1 the detuning starts negative, meaning that the laser wavelength is smaller than the resonance wavelength, and due to the free carrier dispersion it evolves to being positive).

(2) From times 25 ns to 250 ns, the temperature rise due to FCA (caused by the large population of free carriers generated at stage 1) stops the blue shift (remember that, unlike free carrier dispersion, a temperature rise red shifts the resonance wavelength of the modulator). As the temperature continues to rise, the thermal dispersion starts to red shift the resonance of the modulator, pushing the modulator's resonance closer to the laser wavelength. The time scale of this effect is much longer due to the fact that thermal effects are much slower than free carrier effects ($\gamma_{fc} = 1GHz$ compared to $\gamma_{th} = 4MHz$).

(3) From times 250 ns to 320 ns, the increase in temperature eventually reaches the point where the laser wavelength and the resonance wavelength cross again (that is, the wavelength detuning goes from positive to negative sign). In this way, the laser wavelength and the resonance wavelength start to get far from each other and, as a consequence, both the energy stored in the ring and the free carrier population decrease rapidly due to the fact that there's no power getting into the ring.

(4) Finally, the heating of the ring is stopped due to the decrease in the free carrier population (which decreases the FCA), so the temperature starts to decay slowly. As a consequence, the thermal dispersion diminishes, pushing the resonance wavelength and the laser wavelength close again, until eventually the whole cycle starts again.

Figure 4.2 depicts the different steps of the cycle. In short, the induced shift in the resonance wavelength and the nonlinear absorption alter the circulating optical intensity around the ring, which feed back and modify the generation rate of heat and free-carriers.

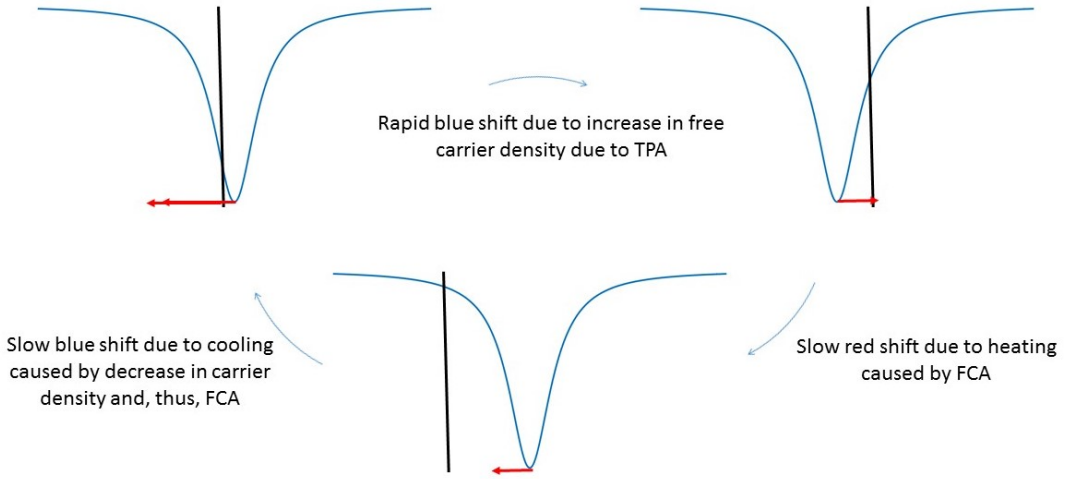

FIGURE 4.2: Self modulation cycle. The black line represents the fixed laser wavelength, and the blue line depicts the modulator resonance that moves due to nonlinear effects. Red arrows show the direction of the resonance shift. A double arrow represents a rapid shift, while a single arrow means slow evolution.

The simulation of this simple case accomplishes two purposes. First, it is a confirmation that the model is correctly derived and simulated numerically, as it reproduces a well-known ring resonator phenomenon. Second, and more importantly, it illustrates the complexity of nonlinearities arising in resonant modulators and the huge effect they can have.

4.4 Power handling capabilities of silicon ring modulators

It is clear that nonlinearities are to be considered when operating resonant modulators with moderately high input powers. From the derivation of the model, it is also apparent that a lot of different parameters play a role in the strength and effects of these

nonlinearities. Mode-averaged parameters that depend on the ring geometry, the bias voltage, the initial detuning between the laser and the resonance of the modulator, the amplitude of the driving voltage... only to mention some of them, are all parameters that affect the nonlinear behavior of the resonator.

As a consequence, all these parameters need to be considered when studying power handling capabilities of resonant modulators. Here, two different categories of parameters affecting nonlinearities are defined and studied separately: (1) design parameters that have to do with the ring dimensions and its doping and (2) operation condition parameters that have to do with the way the modulation is achieved (driving voltage, laser wavelength...).

4.4.1 Design considerations

In a resonant modulator, the design of the ring can have an important impact in the extent of the arising nonlinearities. For instance, a geometry that features a better modal confinement will likely have more intense nonlinearities because the optical power is concentrated in a smaller area, enhancing both TPA and heating.

It is interesting, then, to study how different ring geometries affect the strength of the nonlinear effects. To do so, we first need to differentiate between two different regimes, according to the presence or absence of screening effect[3]:

(1) When there's an applied voltage to the modulator and there's no screening effect, i.e, $P_{in} < 1mW$ for the modulator characterized in chapter 3, the free carrier loss rate γ_{fc} is so high (or, equivalently, the free carrier lifetime so low) that we can disregard the free carrier population, that is, we can assume $N(t) = 0$. Consequently, the only nonlinear effect that effectively plays a role is thermal dispersion due to heating, governed by equation 4.16.

We can consider that γ_{th} will be the same for all the ring geometries, as the heat dissipation is mainly governed by the surroundings of the disk (all the layers of the CMOS process), that are the same regardless of the ring design. In the same way, P_{abs} will be similar for all geometries. We can then reduce the effect geometry has over nonlinearities (in the case of no screening) to the parameter Γ_{disk}/V_{ring}, which can be

[3] See appendix B for a discussion on the screening effect.

easily obtained getting the mode profiles for each geometry using finite elements method (FEM) simulations.

(2) When no voltage is applied to the modulator or the input power is so high that there is screening of the bias electric field ($P_{in} > 1mW$ for our characterized device) the free carrier lifetime is high enough to allow for a considerable free carrier density buildup in the ring, which in turn makes free carrier dispersion important. It is necessary, then, to account for both thermal and free carrier effects.

Equation 4.18 governs the population of free carriers in the ring, and we can argue that γ_{fc} will be the same regardless of the geometry, as it depends mainly on surface recombination which is independent of the ring geometry. We can then reduce the effect of geometry over free carrier nonlinearities to the parameter Γ_{FCA}/V_{FCA}^2, which can again be easily obtained with the mode profiles obtained with FEM simulations.

So, in conclusion, to study the effect different ring geometries have over nonlinearities it is necessary to study two parameters: Γ_{disk}/V_{ring}, that governs the thermal behavior and will be called 'heating parameter', and Γ_{FCA}/V_{FCA}^2, which governs the free carrier nonlinearities and will be called 'free carrier parameter'.

Note that the dependence of the nonlinear parameters with ring dimensions is not obvious due to the fact that these parameters are the quotient of two different variables: the modal confinement Γ and the modal volume V. A decrease in the ring dimensions will likely decrease both Γ and V, so the trend of the value Γ/V when this happens is not clear.

To explore the behavior of nonlinearities with geometry, the two nonlinear parameters were obtained for 510 different ring geometries with varying thicknesses, radii and widths using a custom FEM solver[4]. The different parameter ranges are summarized in table 4.1.

Parameter	*Range*	*Step*	*Units*
radius (r)	$7-15$	1	μm
width (w)	$0.5-3$	0.625	μm
thickness (t)	$80-300$	2.5	nm

TABLE 4.1: Geometrical parameters swept in the ring geometry analysis

[4]See appendix C for the matlab code used.

It is interesting first to see if there is any correlation between the heating parameter and the free carrier parameter. Figure 4.3 shows the scatter plot of these two parameters, in which a strong quadratic correlation is observed. Since an increase in the heating parameter involves an increase in the free carrier parameter and vice versa, we can only analyze one of the two parameters, either the heating parameter or the free carrier parameter, and draw conclusions for both the heating and the free carrier nonlinearities.

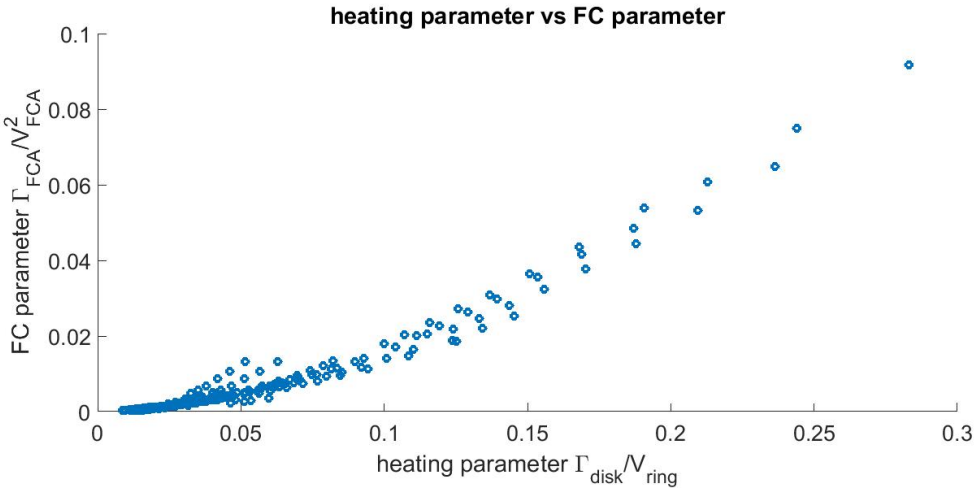

FIGURE 4.3: Free carrier parameter vs heating parameter for all the different simulated geometries.

Figure 4.4 shows the results obtained for a set of the simulated geometries. Figure 4.4(a) shows the dependence of the heating parameter with height and radius for a fixed width, and similarly figure 4.4(b) shows the dependence of the heating parameter with height and width for a fixed radius.

Two main conclusions can be extracted:

(1) Height is the dominant factor affecting the heating parameter: for a fixed height, the evolution with varying radius and width is almost a straight line (meaning that the heating parameter is weakly dependent in these two variables), while the dependence with height is clearly noticeable.

(2) The overall trend of the heating parameter is a reduction with increasing ring volume, meaning that, if nonlinear behavior wants to be avoided, bigger rings have to be designed.

As height is the geometrical parameter that dominates the nonlinear behavior of the ring, it is interesting to further analyze its effect. Figure 4.5 shows the dependence of the heating parameter with varying ring height for a fixed radius and width. Two

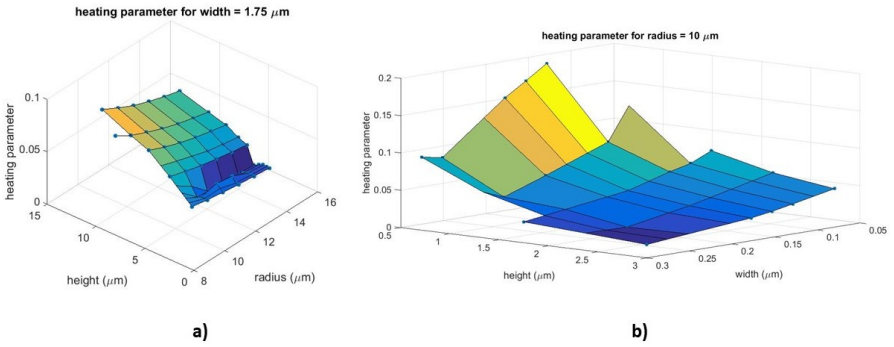

FIGURE 4.4: Heating parameter dependence with geometry. (a) Varying radius and height with fixed width. (b) Varying width and height with fixed radius.

different behaviors are observed: (1) for heights higher than 80 nm, the heating parameter decreases with increasing height, while (2) for heights lower than 80 nm there's an increase in the heating parameter with increasing height.

As the layer heights used in commercial microelectronic foundries span the range 80 nm - 300 nm, to reduce the extent of nonlinearities in zero change CMOS ring structures a high layer thickness (which sets the ring height) is desirable. It is important to note that an increase in the ring height does not change any other relevant parameter affecting the behavior of the device, so reducing the nonlinearities by increasing the ring height does not come at an expense in any other device performance metric.

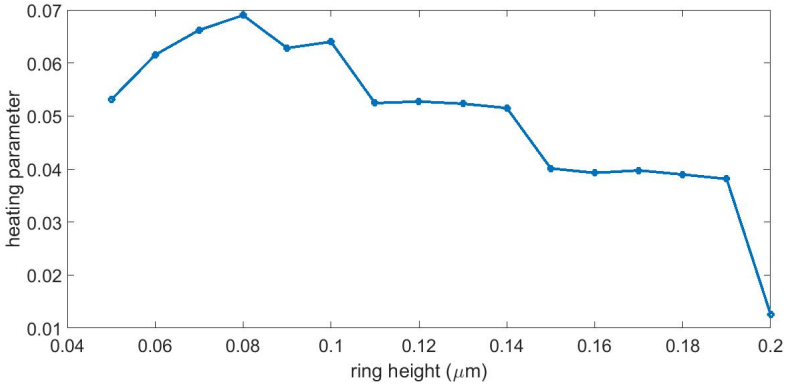

FIGURE 4.5: Heating parameter dependence with varying ring height.

Another design parameter that has an important role in the extent of the nonlinearities is the doping concentration of the p and n regions. The background loss rate γ_{back} increases with increasing doping concentration, and this has two effects: (1) a higher absorbed power P_{abs}, which increases the heating and thus the thermal nonlinearity strength and (2) an increase in the ring losses that affects the maximum energy stored

in the ring U_{max}, which in turn decreases the maximum absorbed power and thus the thermal nonlinearity strength.

As a consequence, it is not obvious which will be the dependence of the nonlinearities with the doping concentration, so the maximum absorbed power P_{abs} was obtained for different doping concentrations using the derived model, assuming equal doping densities at the p and n sides of the junction.

The results are shown in figure 4.6 for two input powers, $3mW$ (so screening of the bias field is assumed) and $1\mu W$ (where there's no screening of the bias field). For both situations a maximum is obtained for doping densities around $2 \times 10^{18} cm^{-3}$, meaning that the thermal nonlinearity strength is higher at these densities. As the free carrier change ΔN (which directly translates into the modulation efficiency through Soref's equations) is proportional to $\sqrt{N_{doping}}$ [20], the use of as much high doping density as possible is beneficial both for reducing the strength of nonlinearities and for increasing the modulation efficiency. The only limitation to the doping density is the amount of optical losses we can afford, as an increase in the doping density increases the losses due to FCA.

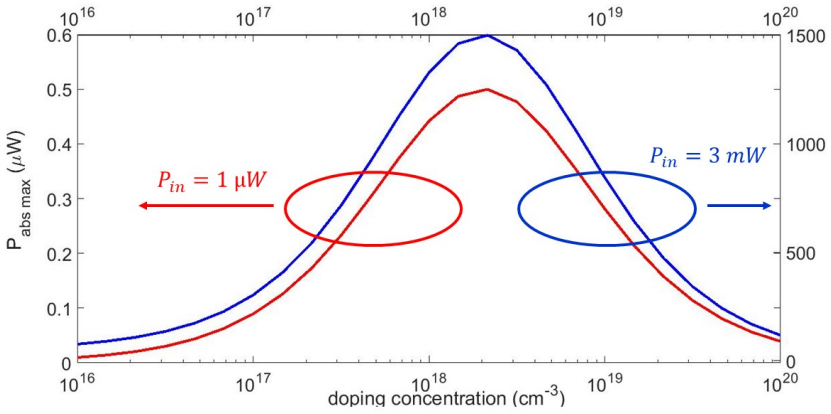

FIGURE 4.6: Maximum absorbed power P_{abs} as a function of doping density for 3 mW and 1 μW input optical powers and $\lambda_l = \lambda_0$. Equal doping for the p and n regions is assumed.

4.4.2 Operation conditions considerations

To study and analyze the power handling capabilities of silicon resonant modulators it is necessary first to come up with a definition of power handling capability. As the final purpose of a modulator is its use for communication, it makes sense to link the power handling capability to a parameter related to the quality of this communication, which leads naturally to the use of the bit error rate (BER).

The BER is the probability of error in detecting a given bit, that is, the probability of detecting a '0' when the bit transmitted was actually a '1' or viceversa. For a simple on-off keying modulation (which is the one used in this thesis), and assuming gaussian statistics for both '0' and '1' values and the use of the optimum decision threshold, the BER can be written as [73]:

$$BER = \frac{1}{2} erfc\left(\frac{Q}{\sqrt{2}}\right) \tag{4.22}$$

where $erfc(x)$ is the complementary error function defined as:

$$erfc(x) = \int_x^\infty e^{-t^2} dt \tag{4.23}$$

and Q is known as the Q-parameter (not to be confused with the Q parameter of a resonance) and is defined as:

$$Q = \frac{\mu_1 - \mu_0}{\sigma_1 + \sigma_0} \tag{4.24}$$

with μ_1 (μ_0) being the mean value of the '1' ('0') bit and σ_1 (σ_0) the variance due to noise. Here, we will consider that the noise (and, as a consequence, σ_1 and σ_0) is independent of the input optical power P_{in} or the operation conditions, such that the BER depends only on the numerator of equation 4.24.

Note that this term can be rewritten in more familiar terms for optical modulators as:

$$\mu_1 - \mu_0 = \frac{P_{in}}{IL}\left(1 - \frac{1}{ER}\right) \tag{4.25}$$

where we have used the fact that $\mu_1 = P_{in}/IL$ and $ER = \mu_1/\mu_0$.

The expression in equation 4.25 constitutes a figure of merit for the performance of the modulator, and as such will be used to compare the different operational conditions considered.

4.4.2.1 The importance of initialization

The presence of nonlinear effects in resonant modulators makes their operation very sensitive to initialization. As one can imagine, the state of the ring when modulation is started (e.g, its temperature, free carrier density...) has an important effect in the modulation characteristics, mainly because it sets the distance between the laser wavelength and the resonance wavelength in which the modulation is going to take place.

It is then of paramount importance for practical and commercial applications to initialize the ring resonance in the best possible way, meaning with this that the best performance can be obtained.

Here, we will consider that, for initialization purposes, the best method is the one which allows to get a smaller '0' transmission value (i.e, μ_0/P_{in}) and still get successful modulation, that is, no instabilities or self modulation take place. The reason for this is that μ_0 is essentially what limits the highest attainable ER[5], meaning that if the initialization method we use is not able to reach near-zero transmission, the achievement of high ER is impossible.

The most immediate way one can think of initializing a modulator is simply by turning on a laser at a specific (optimized) wavelength and start modulating from there. The red curve of figure 4.7(a) shows the minimum attainable transmission (μ_0/P_{in}) using this initialization method for different input powers. While the method is capable of achieving near zero transmission for low input powers (where nonlinearities are very weak), for moderately high input powers near zero transmission is unreachable.

At a first sight this could seem counter-intuitive, because in a critically coupled ring (which is the case considered here) near-zero transmission should be always achievable. But the presence of strong nonlinearities for moderate input powers prevents this in

[5]Note that, if $\mu_0 = 0$, then $ER = \infty$ no matter the value of μ_1.

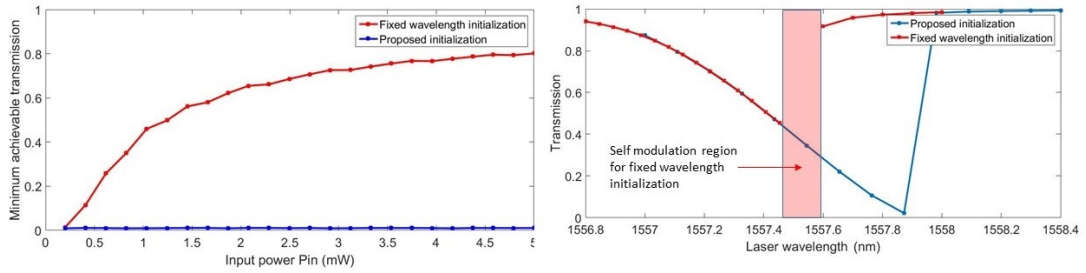

FIGURE 4.7: Comparison between different initialization methods. (a) Minimum achievable transmission as a function of the input power for the fixed wavelength initialization (red) and for the proposed wavelength sweep initialization (blue). (b) Transmission as a function of wavelength for a 1 mW input power for the fixed wavelength initialization (red) and for the proposed initialization (blue). The cold resonance wavelength is set at $\lambda_0 = 1557.2\ nm$.

two different ways, depending on the distance between the laser wavelength and the cold resonance wavelength (i.e, the resonance of the ring when no nonlinear effects are present):

(1) When the laser wavelength is far from the cold resonance wavelength of the ring, the heating pushes the ring resonance even further, thus avoiding the possibility of reaching the transmission dip.

(2) When the laser wavelength is near the cold resonance wavelength of the ring, self modulation due to competing TPA and heating occurs, preventing successful data modulation.

The red curve in figure 4.7(b) shows the transmission as a function of the initialization wavelength for an input power of 1 mW, where the 2 different described behaviors are clearly visible (behavior (2) corresponds to the shaded area, while behavior (1) corresponds to the region to the left of the shaded area). The transition between cases (1) and (2) is very abrupt, confirming the fact that near zero transmission is not achievable using this initialization method.

The derived model and the deep understanding over the physical processes involved allows us to propose an alternative initialization method. By starting the laser wavelength far from the cold resonance of the resonator and sweeping the wavelength (with the laser on) up to a desired value the abrupt change between cases (1) and (2) described above is avoided.

This happens because, although nonlinearities are still present, the generated heating cannot exceed a certain value, so eventually the run-away of the resonator resonance from the laser wavelength due to a temperature increase is stopped. This allows the laser wavelength to get near the resonance of the ring, thus achieving near-zero transmission.

The blue curve of figure 4.7(a) shows the minimum attainable transmissions (μ_0/P_{in}) using the proposed initialization method for different input powers, and a clear improvement in the minimum achievable μ_0 is obtained over all the range of input powers.

The blue curve of figure 4.7(b) shows the evolution of the minimum transmission as the wavelength laser is swept for an input power of 1 mW: as opposed to the fixed wavelength initialization, the wavelength sweep allows to reach the point where no more heating is possible, thus enabling the laser wavelength to approach the resonance wavelength and achieve near-zero transmission.

Therefore, the proposed initialization method has to be used if high performance modulation wants to be obtained under the presence of nonlinearities at high input powers.

4.4.2.2 The best operational point

The initialization method proposed is superior to the others because it allows to reach any desired transmission value, which essentially means that it allows for the achievement of high ER. But the figure of merit derived in equation 4.25 does also account for the IL, so a further study of the operational conditions is needed to find the optimal point.

Note that, essentially, this is equivalent to finding the optimal wavelength at which the initialization method should stop, that is, which should be the final wavelength of the sweep that has to be performed for initialization to get the best data communication.

To obtain the best operational point, the value of the figure of merit defined in equation 4.25 for different stop wavelengths and input powers was obtained using the derived model, and the results are shown in figure 4.8.

Figure 4.8(b) shows the typical evolution of ER, IL and the figure of merit with the stop wavelength of the initialization sweep. Sharp peaks are obtained both for the ER and the IL, but they occur at different wavelengths. The figure of merit also shows a well defined peak at a wavelength that does not correspond to the ER peak nor the IL peak.

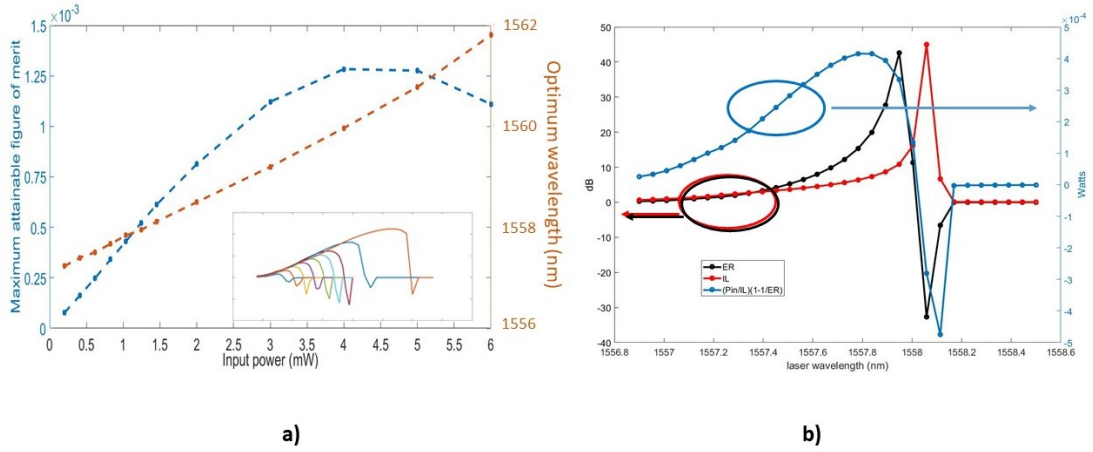

FIGURE 4.8: Optimum operational point. (a) Maximum attainable value of the figure of merit (blue, left axis) and wavelength at which this value is reached (red, right axis) as a function of input power. The inset shows the evolution of the figure of merit as a function of the stop laser wavelength for different input powers. (b) Evolution of the ER (black), IL (red) and figure of merit (black) as a function of the stop laser wavelength. The input power is set to 1 mW, and the cold resonance wavelength is set to $\lambda_0 = 1557.2\ nm$.

This maximum defines the optimal stop wavelength of the initialization that will feature the best data communication performance according to equation 4.25.

Figure 4.8(a) shows the maximum attainable figure of merit and the wavelength at which this maximum occurs for different input powers. Two important conclusions can be extracted: (1) There is a linear relation between the input power and the optimal stop wavelength. (2) There's an optimal input power at which the highest possible performance can be achieved. As can be observed, the maximum attainable figure of merit shows a parabolic dependence with the input power, meaning that a well defined point maximizes the quality of the data communication.

Note that, if nonlinearities were not present in the system, the dependence of the maximum attainable figure of merit with the input power (blue curve in figure 4.8(a)) would be linear, so a higher power would always mean higher performance. The presence of nonlinearities generates the observed parabolic behavior, and as such sets a point where the ring is not able to handle a higher input power and still get better performance. It can be concluded then, that nonlinearities limit the maximum input power a ring resonator can handle, and this limit corresponds to the input power that maximizes the figure of merit, which in case of the modulator characterized in chapter 3 and simulated in this chapter is around 4.5 mW.

4.5 Summary

In this chapter, a complete model of a resonant modulator which incorporates nonlinear effects has been derived and solved numerically.

The effects of the nonlinearities arising in these structures has been discussed, and several techniques to relieve these effects have been proposed.

From a design point of view, it has been shown that an increase in the ring height (that is, in the thickness of the silicon layer) is beneficial in reducing the strength of nonlinearities.

From the operational conditions side, the importance of the initialization method to achieve high performance has been unveiled, and an initialization method that allows the achievement of high ER even for high input powers has been proposed and analyzed. It has also been shown that there exists an optimal operational point that does not correspond neither to the point of highest ER not to the point of minimum IL, and that this optimum point has a linear dependence with the input optical power. It has also been demonstrated that there is a specific input power for which the best performance can be obtained, and this input power sets the power handling limit of the resonant modulator.

By getting a deep understanding of the physical processes involved in the nonlinearities arising in resonant structures and its associated effects and having a model to describe them, better techniques to reduce or even eliminate these undesired phenomena can be proposed and studied. This allows for a much more efficient communication (and also a better signal to noise ratio) with simpler systems by potentially eliminating the need of amplification at the output of these devices.

Chapter 5

Low Temperature Operation of Silicon Microring Modulators

Working at very low (< 10 K) temperatures has several associated benefits, such as low thermal energy (which reduces noise and incoherent interactions) and the dominance of quantum behavior. It is for this reason that a lot of state of the art computers [74] and single photon detectors [75] work at this temperature range.

In particular, superconducting nanowire single photon detectors (SNSPDs) feature high efficiency, low dark counts, excellent timing resolution and even spatial resolution in the visible and infrared region [76], which make them a promising technology for quantum computing, quantum key distribution and space-to-ground communications [77].

One of the main problems with SNSPDs is its readout for communication to ambient temperature systems. The limited cooling power of commercial cryostats requires the minimization of energy flow into the cryogenic environment, and electrical interconnections represent a major challenge, since electrons are hot. To avoid high thermal loads, each electrical connection is thermally anchored at multiple intermediate stages to minimize heating, and numerous levels of electrical filtering and thermalization are necessary [78], which increase the cost and complexity of the system and thus limit the number and bandwidth of these connections.

Optical interconnects offer a promising alternative for cryogenic environment readouts in general, and for SNSPD in particular. By using WDM the number of physical connections to the cryostat is minimized, since more than one signal can propagate through the same fiber. Moreover, the low absorption of optical fiber means less thermal dissipation and, therefore, less thermal load. As a consequence, higher bandwidth, less cryogen consumption and simpler systems can be achieved with optical interconnects.

While optical interconnects for cryogenic readout have already been investigated using hybrid approaches [79], only one work has dealt with the use of silicon photonic modulators for this purpose [80]. As already discussed in this thesis, the use of hybrid approaches prevents an easy integration with CMOS electronics and, moreover, it requires large driving voltages with its associated heating, while silicon photonics provides a low power, low cost and compact solution.

In this chapter, the suitability of the zero change CMOS photonic platform [17] for low temperature applications is evaluated, with special focus on the modulator device because of its paramount importance for cryogenic readout applications.

5.1 Low temperature operation of silicon photonic devices: concerns

Temperature plays a role in almost all the parameters affecting the behavior of a semiconductor, and it is not the purpose nor the scope of this thesis to discuss all of them. In this section, low temperature effects that may prevent a successful operation of photonic devices fabricated in semiconductor substrates in general and silicon in particular are discussed from a theoretical point of view. [81] is left as a reference for a thorough analysis of the temperature effects in semiconductors.

5.1.1 Carrier freeze-out

The main concern for operation of doped semiconductors at cryogenic temperatures is the possibility of carrier freeze-out. At room temperature, it is always assumed that all the impurities are ionized, such that the free carrier density is approximately equal to the impurity concentration. When the temperature is lowered, this assumption does not hold

anymore, and considerably less than 100% ionization occurs. At temperatures near the absolute 0, there's nearly no ionization, so the number of free carriers is negligibly small. This is known as carrier freeze-out [81, 82], an effect that would completely hamper the suitability of photonic devices involving free carriers for cryogenic operation.

Nonetheless, carrier freeze-out can be overcome if the semiconductor is sufficiently doped: at high doping densities, the Fermi level lies either in the conduction or the valence band, causing the material to behave as a metal: the impurities are so close that they form an impurity band where conduction of free carriers is possible, in what is known as the Mott metal-insulator transition [83]. For silicon, this transition occurs at densities around $4 \times 10^{18}\ cm^{-3}$ [84]. Carrier freeze-out, then, should not be a concern for sufficiently high impurity concentrations.

5.1.2 Modulation considerations

With all the effects that low temperatures have in silicon, it is not completely clear that, even if there's no carrier freezeout, modulation through the plasma dispersion effect can be achieved at this temperature range.

As already mentioned, the plasma dispersion effect can be approximated using a Drude model [10], which yields the following equations valid for all temperatures:

$$\Delta n = -\frac{e^2\lambda_0^2}{8\pi^2 c^2 \varepsilon_0 n}\left(\frac{\Delta N_e}{m^*_{ce}} + \frac{\Delta N_h}{m^*_{ch}}\right) \tag{5.1}$$

$$\Delta \alpha = \frac{e^3\lambda_0^2}{4\pi^2 c^3 \varepsilon_0 n}\left(\frac{\Delta N_e}{\mu_e (m^*_{ce})^2} + \frac{\Delta N_h}{\mu_h (m^*_{ch})^2}\right) \tag{5.2}$$

where m^*_{ce} (m^*_{ch}) is the conductivity effective mass for electrons (holes) and μ_e (μ_h) is the mobility for the electrons (holes). Note that the Drude model is not exact at room temperature, where Soref's empirical equations are used, but it is good enough for estimation purposes.

The only temperature dependent parameters in equations 5.1 and 5.2 are the mobility and effective masses of holes and electrons, which have been reported in the literature for silicon at low and room temperatures. These values are summarized in table 5.1.

Parameter	$T = 4K$	*room T*
m^*_{ce}	$0.26m_0$ [85]	$0.273m_0$ [85]
m^*_{ch}	$0.334m_0$ [85]	$0.367m_0$ [85]
μ_e $(cm^2/V \cdot s)$	< 20 [86]	280 [87]
μ_h $(cm^2/V \cdot s)$	< 10 [86]	100 [87]

TABLE 5.1: Hole and electron conductivity effective masses (in units of the free electron mass m_0) and mobilities (in $cm^2/V \cdot s$) in silicon at 4K and 300K for doping densities $N_a = N_d = 1 \times 10^{18}$ cm^{-3}.

As the effective masses of both electrons and holes are similar at room temperature and 4K, the change in the refractive index Δn should be very similar at both operating temperatures, being slightly better at low temperatures due to reduced effective masses. In principle, then, the modulation efficiency should stay the same regardless of temperature, allowing for successful modulation also at cryogenic temperatures.

The carrier mobilities are much smaller for low temperatures, thus the change in optical losses $\Delta\alpha$ should be much higher for this operating conditions. A higher change in $\Delta\alpha$ does not directly affect the modulation performance of the device, but it induces a higher chirp to the signal, which could be detrimental for long distance transmission.

5.2 IV characteristics

As discussed, carrier freeze-out is a concern for the operation of silicon photonics devices at cryogenic temperatures, but it can be overcome with a sufficiently high doping density.

As a preliminary measurement to ensure that carrier freeze-out does not happen in the devices fabricated using the zero-change CMOS approach, IV curves of the modulator characterized in chapter 2 were taken at different temperatures.

The results are shown in figure 5.1. A diode-like IV curve is obtained at all test temperatures. The presence of a high ($\sim mA$) current at forward bias implies no carrier freeze-out happens even at temperatures as low as 4K. This constitutes a first proof that the photonic devices fabricated using the zero-change CMOS approach can be readily used for low temperature applications.

Note the increase in the turn-on voltage of the diode with decreasing temperature. This is due to an increase in the diode's built-in potential caused by the shift of the Fermi level towards the dopant (or acceptor) energy level.

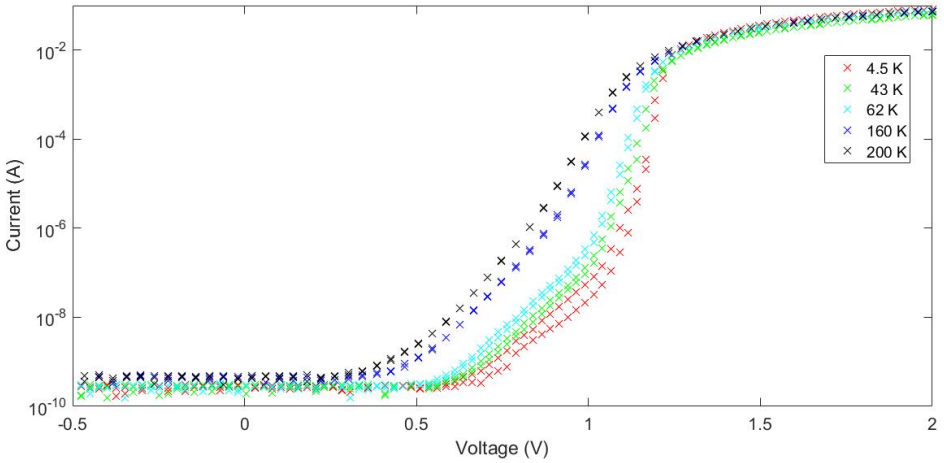

FIGURE 5.1: IV characteristics of a 1550 nm zero-change CMOS microring modulator at different temperatures. Diode-like characteristics are obtained at all tested temperatures.

IV curves were also obtained for other photonic devices fabricated with the zero-change CMOS approach, such as 1180 nm modulators and photodetectors, yielding similar results.

It is important to stress the relevance of the obtained results, since a diode-like behavior at these low temperatures means that the zero change CMOS photonic platform (including waveguides, modulators and photodetectors) can be used for cryogenic applications without any further modification.

5.3 Summary

In this chapter the potential of the zero change CMOS photonic platform for low temperature applications has been discussed, both from the theoretical and experimental point of view.

A theoretical analysis concludes that the effects low temperature has over the behavior of silicon should not prevent the successful operation of silicon photonic devices, and these effects could even be beneficial in terms of modulation efficiency, noise and nonlinear behavior.

The absence of carrier freeze-out due to high doping concentrations has been demonstrated by the acquisition of IV curves at low temperatures, in which a diode-like behavior over the whole tested temperature range (4K to room temperature) and for all the different photonic components (modulators and photodetectors) is obtained.

Altogether, this represents a first proof of the suitability of the zero change CMOS photonic platform for low temperature applications without the need of any further modification.

Chapter 6

Conclusions and future work

Multiple interesting conclusions, as well as different future research directions, constitute the result of this thesis.

In chapter 3, the high speed characterization of a zero-change CMOS microring modulator fabricated in thin silicon for a 1550 nm working wavelength has been reported for the first time. 20 pm/V modulation efficiency and 14 GHz bandwidth has been demonstrated, allowing for high speed modulation up to 32 Gbps, as well as moderate (50 - 75 Km) distance data transmission without dispersion compensation.

Future work in this regard would include the characterization of the achievable BER of the device as well as the power penalty after transmission over SMF. This would require the fabrication of new devices with grating couplers optimized for 1550 nm to avoid high losses and its associated detrimental effects in the signal to noise ratio.

In chapter 4, a complete model of a silicon resonant modulator, including its nonlinear behavior, has been derived, simulated and studied. The model has been used to propose important design practices to reduce and even avoid the undesired nonlinear effects arising as a result of the high energy buildup occurring in resonant structures. An initialization method that allows the achievement of high ER even in the presence of strong nolinearities has been proposed, and the existence of an optimal operational point for both the input optical power and the laser wavelength has been demonstrated.

The derived model constitutes a full description of the behavior of a general resonant structure and, as such, its applications may go beyond the analysis of silicon modulators

and could be applied to other interesting resonant structures such as photodetectors or cavities for nonlinear optics. Future work could be, then, applying the model to these to make a similar analysis.

In chapter 5, preliminary theoretical and experimental work to evaluate the suitability of the zero change CMOS photonic platform for low temperature applications has been performed, concluding that, in principle, it could be successfully used without any further change to the fabrication or design process.

The next step to confirm the suitability of the zero change CMOS photonic platform to be operated at cryogenic temperatures would be to test, at these temperatures, their performance at high data rates. This means, essentially, the realization of the same characterization presented in chapter 2 but in a cryogenic environment.

At a bigger picture, this thesis has demonstrated the extension of the zero change CMOS platform to 1550 nm working wavelengths and to low temperature regimes, demonstrating the validity of the zero change CMOS approach to build cheap, high performance electronic-photonic systems. Not only this, but it also constitutes the first thorough analysis of power handling capabilities in silicon resonant modulators, giving a useful tool for the study of its nonlinear behavior.

At this broader perspective, several future research directions can be proposed. For example, the analysis in chapter 4 revealed the fact that thin silicon layers are indeed the ones leading to higher nonlinearities, which suggest the possibility of using the zero change CMOS approach for doing nonlinear optics more efficiently. More generally, the large scale commercial adoption of silicon photonics still has to overcome several major limitations, such as efficient light coupling in and out of the chip, the realization of efficient laser sources in silicon, or the increase in the integrated photonic devices performance.

Bibliography

[1] E. Mounier and J. Malinge. Silicon photonics for data centers and other applications. Technical report, Yole Développement, 2016.

[2] C. Sun, M. T. Wade, Y. Lee, J. S. Orcutt, L. Alloatti, M. S. Georgas, A. S. Waterman, J. M. Shainline, R. R. Avizienis, S. Lin, B. R. Moss, R. Kumar, F. Pavanello, A. H. Atabaki, H. M. Cook, A. J. Ou, J. C. Leu, Y. Chen, K. Asanovic, R. J. Ram, M. A. Popovic, and V. M. Stojanovic. Single-chip microprocessor that communicates directly using light. *Nature*, 528:534–538, 2015. doi: 10.1038/nature16454.

[3] G. T. Reed, G. Mashanovich, F. Y. Gardes, and D. J. Thomson. Silicon optical modulators. *Nature Photonics*, 4:518–526, July 2010. doi: 10.1038/nphoton.2010.179.

[4] M. T. Wade, Jeffrey M. S., J. S. Orcutt, R. J. Ram, V. Stojanovic, and M. A. Popovic. Spoked-ring microcavities: enabling seamless integration of nanophotonics in unmodified advanced CMOS microelectronics chips. In *Proc. SPIE*, volume 8991, pages 89910B–89910B–8, 2014. doi: 10.1117/12.2054788.

[5] Q. Xu, B. Schmidt, S. Pradhan, and M. Lipson. Micrometre-scale silicon electro-optic modulator. *Nature*, 435:325–327, February 2005. doi: 10.1038/nature03569.

[6] G. T. Reed, G. Z. Mashanovich, F. Y. Gardes, M. Nedeljkovic, Y. Hu, D. J. Thomson, K. Li, P. R. Wilson, S. Chen, and S. S. Hsu. Recent breakthroughs in carrier depletion based silicon optical modulators. *Nanophotonics*, 3(4-5):1–18, January 2014. doi: 10.1515/nanoph-2013-0016.

[7] D. A. B. Miller. Rationale and challenges for optical interconnects to electronic chips. *Proceedings of the IEEE*, 88(6):728–749, June 2000. ISSN 0018-9219. doi: 10.1109/5.867687.

[8] J. W. Goodman, F. J. Leonberger, S. Kung, and R. A. Athale. Optical interconnections for VLSI systems. *Proceedings of the IEEE*, 72(7):850–866, July 1984. ISSN 0018-9219. doi: 10.1109/PROC.1984.12943.

[9] S. E. Miller. Integrated optics: An introduction. *Bell System Technical Journal*, 48 (7):2059–2069, 1969. ISSN 1538-7305. doi: 10.1002/j.1538-7305.1969.tb01165.x.

[10] G. T. Reed and A. P. Knights. *Silicon Photonics: An Introduction*. John Wiley & Sons Ltd, The Atrium, Southern Gate, Chichester, West Sussex PO19 8SQ, England, first edition, 2004.

[11] R. A. Soref and J. P. Lorenzo. Single-crystal silicon: a new material for 1.3 and 1.6 μm integrated-optical components. *Electronics Letters*, 21(21):953–954, October 1985. ISSN 0013-5194. doi: 10.1049/el:19850673.

[12] F. Boeuf, S. Cremer, E. Temporiti, M. Fere, M. Shaw, N. Vulliet, B. Orlando, D. Ristoiu, A. Farcy, T. Pinguet, A. Mekis, G. Masini, P. Sun, Y. Chi, H. Petiton, S. Jan, J. R. Manouvrier, C. Baudot, P. Le Maitre, J. F. Carpentier, L. Salager, M. Traldi, L. Maggi, D. Rigamonti, C. Zaccherini, C. Elemi, B. Sautreuil, and L. Verga. Recent progress in silicon photonics R&D and manufacturing on 300mm wafer platform. In *2015 Optical Fiber Communications Conference and Exhibition (OFC)*, pages 1–3, March 2015.

[13] C. Doerr, L. Chen, D. Vermeulen, T. Nielsen, S. Azemati, S. Stulz, G. McBrien, X. M. Xu, B. Mikkelsen, M. Givehchi, C. Rasmussen, and S. Y. Park. Single-chip silicon photonics 100-Gb/s coherent transceiver. In *OFC 2014*, pages 1–3, March 2014. doi: 10.1364/OFC.2014.Th5C.1.

[14] D. Liang and J. E. Bowers. Recent progress in lasers on silicon. *Nature Photonics*, 4:511–517, July 2010. doi: 10.1038/nphoton.2010.167.

[15] J. Leuthold, C. Koos, and W. Freude. Nonlinear silicon photonics. *Nature Photonics*, 4:535 – 544, July 2010. doi: 10.1038/nphoton.2010.185.

[16] M. J. R. Heck, H. W. Chen, A. W. Fang, B. R. Koch, D. Liang, H. Park, M. N. Sysak, and J. E. Bowers. Hybrid silicon photonics for optical interconnects. *IEEE Journal of Selected Topics in Quantum Electronics*, 17(2):333–346, March 2011. ISSN 1077-260X. doi: 10.1109/JSTQE.2010.2051798.

[17] J. S. Orcutt, B. Moss, C. Sun, J. Leu, M. Georgas, J. Shainline, E. Zgraggen, H. Li, J. Sun, M. Weaver, S. Urošević, M. Popović, R. J. Ram, and V. Stojanović. Open foundry platform for high-performance electronic-photonic integration. *Opt. Express*, 20(11):12222–12232, May 2012. doi: 10.1364/OE.20.012222.

[18] L. Alloatti, D. Cheian, and R. J. Ram. High-speed modulator with interleaved junctions in zero-change CMOS photonics. *Applied Physics Letters*, 108(13):131101, 2016. doi: 10.1063/1.4944999.

[19] A. H. Atabaki, H. Meng, L. Alloatti, K. K. Mehta, and R. J. Ram. High-speed polysilicon CMOS photodetector for telecom and datacom. *Applied Physics Letters*, 109(11):111106, 2016. doi: 10.1063/1.4962641.

[20] S. M. Sze and K. K. Ng. *Physics of Semiconductor Devices*. John Wiley & Sons Ltd, The Atrium, Southern Gate, Chichester, West Sussex PO19 8SQ, England, third edition, 2006.

[21] H. A. Hauss. *Waves and Fields in Optoelectronics*. Solid state physical electronics. Prentice Hall, Englewood Cliffs, New Jersey 07632, second edition, 1984.

[22] C. Xiong, D. Gill, J. Proesel, J. Orcutt, W. Haensch, and W. M. J. Green. A monolithic 56 Gb/s CMOS integrated nanophotonic PAM-4 transmitter. In *2015 IEEE Optical Interconnects Conference (OI)*, pages 16–17, April 2015. doi: 10.1109/OIC.2015.7115665.

[23] T. Barwicz, H. Byun, F. Gan, C. W. Holzwarth, M. A. Popovic, P. T. Rakich, M. R. Watts, E. P. Ippen, F. X. Kärtner, H. I. Smith, J. S. Orcutt, R. J. Ram, V. Stojanovic, O. O. Olubuyide, J. L. Hoyt, S. Spector, M. Geis, M. Grein, T. Lyszczarz, and J. U. Yoon. Silicon photonics for compact, energy-efficient interconnects. *J. Opt. Netw.*, 6(1):63–73, January 2007. doi: 10.1364/JON.6.000063.

[24] R. Soref and B. Benett. Electrooptical effects in silicon. *IEEE J. Quantum Elect*, QE-23:123–129, January 1987.

[25] G.V. Treyz. Silicon Mach-Zehnder waveguide interferometers operating at 1.3 μm. *Electronic Letters*, 27 (2):118–120, January 1991.

[26] G. V. Treyz, P. G. May, and JeanMarc Halbout. Silicon Mach-Zehnder waveguide interferometers based on the plasma dispersion effect. *Applied Physics Letters*, 59 (7):771–773, 1991. doi: 10.1063/1.105338.

[27] D. G. Rabus. *Ring Resonators: Theory and Modeling*, pages 3–40. Springer Berlin Heidelberg, Berlin, Heidelberg, 2007. ISBN 978-3-540-68788-7. doi: 10.1007/978-3-540-68788-7_2.

[28] Z. Wang, Y. Gao, A. S. Kashi, J. C. Cartledge, and A. P. Knights. Silicon microring modulator for dispersion uncompensated transmission applications. *J. Lightwave Technol.*, 34(16):3675–3681, August 2016.

[29] G. Li, A. V. Krishnamoorthy, I. Shubin, J. Yao, Y. Luo, H. Thacker, X. Zheng, K. Raj, and J. E. Cunningham. Ring resonator modulators in silicon for interchip photonic links. *IEEE Journal of Selected Topics in Quantum Electronics*, 19(6): 95–113, November 2013. ISSN 1077-260X. doi: 10.1109/JSTQE.2013.2278885.

[30] R. A. Soref and B. R. Bennett. Kramers-kronig analysis of electro-optical switching in silicon. In *Proc. SPIE*, volume 0704, pages 32–37, 1987. doi: 10.1117/12.937193.

[31] C. K. Tang and G. T. Reed. Highly efficient optical phase modulator in SOI waveguides. *Electronics Letters*, 31(6):451–452, March 1995. ISSN 0013-5194. doi: 10.1049/el:19950328.

[32] C. E. Png, S. P. Chan, S. T. Lim, and G. T. Reed. Optical phase modulators for MHz and GHz modulation in silicon-on-insulator (SOI). *Journal of Lightwave Technology*, 22(6):1573–1582, June 2004. ISSN 0733-8724. doi: 10.1109/JLT.2004.827655.

[33] F. Y. Gardes, G. T. Reed, N.G. Emerson, and C.E. Png. A sub-micron depletion-type photonic modulator in silicon on insulator. *Opt. Express*, 13(22):8845–8854, October 2005. doi: 10.1364/OPEX.13.008845.

[34] A. Liu, L. Liao, D. Rubin, H. Nguyen, B. Ciftcioglu, Y. Chetrit, N. Izhaky, and M. Paniccia. High-speed optical modulation based on carrier depletion in a silicon waveguide. *Opt. Express*, 15(2):660–668, January 2007. doi: 10.1364/OE.15.000660.

[35] C. E. Png. *Silicon-on-insulator phase modulators*. PhD thesis, University of Surrey, 2004.

[36] D. M. Gill, M. Rasras, K. Y. Tu, Y. K. Chen, A. E. White, S. S. Patel, D. Carothers, A. Pomerene, R. Kamocsai, C. Hill, and J. Beattie. Internal bandwidth equalization in a CMOS-compatible Si-ring modulator. *IEEE Photonics Technology Letters*, 21 (4):200–202, February 2009. ISSN 1041-1135. doi: 10.1109/LPT.2008.2009943.

[37] E. Timurdogan, C. M. Sorace-Agaskar, J. Sun, E. S. Hosseini, A. Biberman, and M. R. Watts. An ultralow power athermal silicon modulator. *Nature Communications*, 5, June 2014. doi: 10.1038/ncomms5008.

[38] J. You, M. Park, J. Park, and G. Kim. 12.5 Gbps optical modulation of silicon racetrack resonator based on carrier-depletion in asymmetric p-n diode. *Opt. Express*, 16(22):18340–18344, October 2008. doi: 10.1364/OE.16.018340.

[39] J. C. Rosenberg, W. M. J. Green, S. Assefa, D. M. Gill, T. Barwicz, M. Yang, S. M. Shank, and Y. A. Vlasov. A 25 Gbps silicon microring modulator based on an interleaved junction. *Opt. Express*, 20(24):26411–26423, November 2012. doi: 10.1364/OE.20.026411.

[40] H. Yu, M. Pantouvaki, P. Verheyen, G. Lepage, P. Absil, W. Bogaerts, and J. Van Campenhout. Silicon dual-ring modulator driven by differential signal. *Opt. Lett.*, 39(22):6379–6382, November 2014. doi: 10.1364/OL.39.006379.

[41] Y. Li, L. Zhang, M. Song, B. Zhang, J. Yang, R. G. Beausoleil, A. E. Willner, and P. D. Dapkus. Coupled-ring-resonator-based silicon modulator for enhanced performance. *Opt. Express*, 16(17):13342–13348, August 2008. doi: 10.1364/OE.16.013342.

[42] D. M. Gill, S. S. Patel, M. Rasras, K. Tu, A. E. White, Y. Chen, A. Pomerene, D. Carothers, R. L. Kamocsai, C. M. Hill, and J. Beattie. CMOS-compatible Si-ring-assisted Mach-Zehnder interferometer with internal bandwidth equalization. *IEEE Journal of Selected Topics in Quantum Electronics*, 16(1):45–52, January 2010.

[43] W. D. Sacher, W. Green, S. Assefa, T. Barwicz, H. Pan, S. Shank, Y. Vlasov, and J. Poon. 28 Gb/s silicon microring modulation beyond the linewidth limit by coupling modulation. In *Optical Fiber Communication Conference*, page OM3J.2. Optical Society of America, 2012. doi: 10.1364/OFC.2012.OM3J.2.

[44] H. Chen, Y. Kuo, and J. E. Bowers. 25Gb/s hybrid silicon switch using a capacitively loaded traveling wave electrode. *Opt. Express*, 18(2):1070–1075, January 2010. doi: 10.1364/OE.18.001070.

[45] J. Liu, D. Pan, S. Jongthammanurak, K. Wada, L. C. Kimerling, and J. Michel. Design of monolithically integrated GeSi electro-absorption modulators and photodetectors on an SOI platform. *Opt. Express*, 15(2):623–628, January 2007. doi: 10.1364/OE.15.000623.

[46] A. N. Oraevsky. Whispering-gallery waves. *Quantum Electronics*, 32(5):377, 2002.

[47] M. T. Wade, F. Pavanello, R. Kumar, C. M. Gentry, A. Atabaki, R. Ram, V. Stojanovi, and M. A. Popovi. 75 % efficient wide bandwidth grating couplers in a 45 nm microelectronics CMOS process. In *2015 IEEE Optical Interconnects Conference (OI)*, pages 46–47, April 2015. doi: 10.1109/OIC.2015.7115679.

[48] X. Xiao, H. Xu, X. Li, Y. Hu, K. Xiong, Z. Li, T. Chu, Y. Yu, and J. Yu. 25 Gbit/s silicon microring modulator based on misalignment-tolerant interleaved pn junctions. *Opt. Express*, 20(3):2507–2515, January 2012. doi: 10.1364/OE.20.002507.

[49] A. Biberman, S. Manipatruni, N. Ophir, L. Chen, M. Lipson, and K. Bergman. First demonstration of long-haul transmission using silicon microring modulators. *Opt. Express*, 18(15):15544–15552, July 2010. doi: 10.1364/OE.18.015544.

[50] W. A. Zortman, A. L. Lentine, M. R. Watts, and D. C. Trotter. Power penalty measurement and frequency chirp extraction in silicon microdisk resonator modulators. In *2010 Conference on Optical Fiber Communication (OFC/NFOEC), collocated National Fiber Optic Engineers Conference*, pages 1–3, March 2010. doi: 10.1364/OFC.2010.OMI7.

[51] F. Koyama and K. Iga. Frequency chirping in external modulators. *Journal of Lightwave Technology*, 6(1):87–93, January 1988. ISSN 0733-8724. doi: 10.1109/50.3969.

[52] P. Henry. Lightwave primer. *IEEE Journal of Quantum Electronics*, 21(12):1862–1879, December 1985. ISSN 0018-9197. doi: 10.1109/JQE.1985.1072601.

[53] F. Devaux, Y. Sorel, and J. F. Kerdiles. Simple measurement of fiber dispersion and of chirp parameter of intensity modulated light emitter. *Journal of Lightwave*

Technology, 11(12):1937–1940, December 1993. ISSN 0733-8724. doi: 10.1109/50.257953.

[54] L. Zhang, Y. Li, J. Y. Yang, M. Song, R. G. Beausoleil, and A. E. Willner. Silicon-based microring resonator modulators for intensity modulation. *IEEE Journal of Selected Topics in Quantum Electronics*, 16(1):149–158, January 2010. ISSN 1077-260X. doi: 10.1109/JSTQE.2009.2027816.

[55] J. C. Cartledge. Comparison of effective α-parameters for semiconductor Mach-Zehnder optical modulators. *J. Lightwave Technol.*, 16(3):372, March 1998.

[56] K. Padmaraju, D. F. Logan, X. Zhu, J. J. Ackert, A. P. Knights, and K. Bergman. Integrated thermal stabilization of a microring modulator. *Opt. Express*, 21(12):14342–14350, June 2013. doi: 10.1364/OE.21.014342.

[57] M. Dinu, F. Quochi, and H. Garcia. Third-order nonlinearities in silicon at telecom wavelengths. *Applied Physics Letters*, 82(18):2954–2956, 2003. doi: 10.1063/1.1571665.

[58] V. R. Almeida and M. Lipson. Optical bistability on a silicon chip. *Opt. Lett.*, 29 (20):2387–2389, October 2004. doi: 10.1364/OL.29.002387.

[59] Q. Xu and M. Lipson. Carrier-induced optical bistability in silicon ring resonators. *Opt. Lett.*, 31(3):341–343, February 2006. doi: 10.1364/OL.31.000341.

[60] T. J. Johnson, M. Borselli, and O. Painter. Self-induced optical modulation of the transmission through a high-Q silicon microdisk resonator. *Opt. Express*, 14(2):817–831, January 2006. doi: 10.1364/OPEX.14.000817.

[61] J. Leuthold, C. Koos, and W. Freude. Nonlinear silicon photonics. *Nature photonics*, 4:535 – 544, July 2010. doi: 10.1038/nphoton.2010.185.

[62] Q. Lin, Oskar J. Painter, and Govind P. Agrawal. Nonlinear optical phenomena in silicon waveguides: Modeling and applications. *Opt. Express*, 15(25):16604–16644, December 2007. doi: 10.1364/OE.15.016604.

[63] T. K. Liang and H. K. Tsang. Efficient raman amplification in silicon-on-insulator waveguides. *Applied Physics Letters*, 85(16):3343–3345, 2004. doi: 10.1063/1.1807960.

[64] D. J. Moss, L. Fu, I. Littler, and B. J. Eggleton. Ultrafast all-optical modulation via two-photon absorption in silicon-on-insulator waveguides. *Electronics Letters*, 41(6):320–321, March 2005. ISSN 0013-5194. doi: 10.1049/el:20058051.

[65] H. K. Tsang, C. S. Wong, T. K. Liang, I. E. Day, S. W. Roberts, A. Harpin, J. Drake, and M. Asghari. Optical dispersion, two-photon absorption and self-phase modulation in silicon waveguides at 1.5m wavelength. *Applied Physics Letters*, 80 (3):416–418, 2002. doi: 10.1063/1.1435801.

[66] S. F. Preble, Q. Xu, and M. Lipson. Changing the colour of light in a silicon resonator. *Nature Photonics*, 1:293–296, 2007. doi: 10.1038/nphoton.2007.72.

[67] B. E. Little, S. T. Chu, H. A. Haus, J. Foresi, and J. P. Laine. Microring resonator channel dropping filters. *Journal of Lightwave Technology*, 15(6):998–1005, June 1997. ISSN 0733-8724. doi: 10.1109/50.588673.

[68] P. E. Barclay, K. Srinivasan, and O. Painter. Nonlinear response of silicon photonic crystal microresonators excited via an integrated waveguide and fiber taper. *Opt. Express*, 13(3):801–820, February 2005. doi: 10.1364/OPEX.13.000801.

[69] J. T. Robinson, K. Preston, O. Painter, and M. Lipson. First-principle derivation of gain in high-index-contrast waveguides. *Opt. Express*, 16(21):16659–16669, October 2008. doi: 10.1364/OE.16.016659.

[70] Dinis Cheian. T-junction resonant modulators and detectors in CMOS. Master's thesis, Massachusetts Institute of Technology, 2016.

[71] https://www.synopsys.com/silicon/tcad.html.

[72] T. Carmon, L. Yang, and K. J. Vahala. Dynamical thermal behavior and thermal self-stability of microcavities. *Opt. Express*, 12(20):4742–4750, October 2004. doi: 10.1364/OPEX.12.004742.

[73] G. P. Agrawal. *Fiber-Optic Communication Systems*. John Wiley & Sons, Inc., 2011. ISBN 9780470918524. doi: 10.1002/9780470918524.

[74] K. K. Likharev and V. K. Semenov. Rsfq logic/memory family: a new josephson-junction technology for sub-terahertz-clock-frequency digital systems. *IEEE Transactions on Applied Superconductivity*, 1(1):3–28, March 1991. ISSN 1051-8223. doi: 10.1109/77.80745.

[75] R. H. Hadfield. Single-photon detectors for optical quantum information applications. *Nature photonics*, 3:696–705, November 2009. doi: 10.1038/nphoton.2009.230.

[76] Q. Zhao, D. Zhu, N. Calandri, A. E. Dane, A. N. McCaughan, F. Bellei, H. Wang, D. F. Santavicca, and K. K. Berggren. Single-photon imager based on a superconducting nanowire delay line. *Nature photonics*, 11:247251, March 2017. doi: 10.1038/nphoton.2017.35.

[77] C. M. Natarajan, M. G. Tanner, and R. H. Hadfield. Superconducting nanowire single-photon detectors: physics and applications. *Superconductor Science and Technology*, 25(6):063001, March 2012. doi: 10.1088/0953-2048/25/6/063001.

[78] F. Kuemmeth and C. M. Marcus. Reducing noise and temperature during measurements in cryostats, March 2015. US Patent App. 14/011,176.

[79] B. Lu, Y. Lu, J. Cheng, R. P. Schneider, J. C. Zolper, and G. Goncher. Gigabit-per-second cryogenic optical link using optimized low-temperature AlGaAs-GaAs vertical-cavity surface-emitting lasers. *IEEE Journal of Quantum Electronics*, 32 (8):1347–1359, August 1996. ISSN 0018-9197. doi: 10.1109/3.511547.

[80] M. Gehl, C. Long, D. Trotter, A. Starbuck, A. Pomerene, J. B. Wright, S. Melgaard, J. Siirola, A. L. Lentine, and C. DeRose. Operation of high-speed silicon photonic micro-disk modulators at cryogenic temperatures. *Optica*, 4(3):374–382, March 2017. doi: 10.1364/OPTICA.4.000374.

[81] V. K. Khanna. Temperature effects on semiconductors. In *Extreme-Temperature and Harsh-Environment Electronics*, 2053-2563, pages 3–1 to 3–33. IOP Publishing, 2017. ISBN 978-0-7503-1155-7. doi: 10.1088/978-0-7503-1155-7ch3.

[82] A. Akturk, J. Allnutt, Z. Dilli, N. Goldsman, and M. Peckerar. Device modeling at cryogenic temperatures: Effects of incomplete ionization. *IEEE Transactions on Electron Devices*, 54(11):2984–2990, November 2007. ISSN 0018-9383. doi: 10.1109/TED.2007.906966.

[83] N. F. Mott. Metal-insulator transition. *Rev. Mod. Phys.*, 40:677–683, October 1968. doi: 10.1103/RevModPhys.40.677.

[84] T. F. Rosenbaum, K. Andres, G. A. Thomas, and R. N. Bhatt. Sharp Metal-Insulator Transition in a Random Solid. *Physical Review Letters*, 45:1723–1726, November 1980. doi: 10.1103/PhysRevLett.45.1723.

[85] D. M. Riffe. Temperature dependence of silicon carrier effective masses with application to femtosecond reflectivity measurements. *J. Opt. Soc. Am. B*, 19(5): 1092–1100, May 2002. doi: 10.1364/JOSAB.19.001092.

[86] F. J. Morin and J. P. Maita. Electrical properties of silicon containing arsenic and boron. *Phys. Rev.*, 96:28–35, October 1954. doi: 10.1103/PhysRev.96.28.

[87] C. Jacoboni, C. Canali, G. Ottaviani, and A. Alberigi Quaranta. A review of some charge transport properties of silicon. *Solid-State Electronics*, 20(2):77 – 89, 1977. ISSN 0038-1101. doi: 10.1016/0038-1101(77)90054-5.